
PHYSICS-INFORMED NEURAL NETWORKS FOR SOURCE INVERSION AND PARAMETERS ESTIMATION IN ATMOSPHERIC DISPERSION

Brenda Anague

School of Agriculture and Science
University of KwaZulu-Natal
Pietermaritzburg, SA 3201

&

AIMS RIC
Kigali, Rwanda

Bamdad Hosseini

Department of Applied Mathematics
University of Washington
Seattle, WA, USA

Issa Karambal

AIMS RIC
Kigali, Rwanda

Jean Medard Ngotchouye
School of Agriculture and Science
University of KwaZulu-Natal
Pietermaritzburg, SA 3201

December 9, 2025

ABSTRACT

Recent studies have shown the success of deep learning in solving forward and inverse problems in engineering and scientific computing domains, such as physics-informed neural networks (PINNs). In the fields of atmospheric science and environmental monitoring, estimating emission source locations is a central task that further relies on multiple model parameters that dictate velocity profiles and diffusion parameters. Estimating these parameters at the same time as emission sources from scarce data is a difficult task. In this work, we achieve this by leveraging the flexibility and generality of PINNs. We use a weighted adaptive method based on the neural tangent kernels to solve a source inversion problem with parameter estimation on the 2D and 3D advection-diffusion equations with unknown velocity and diffusion coefficients that may vary in space and time. Our proposed weighted adaptive method is presented as an extension of PINNs for forward PDE problems to a highly ill-posed source inversion and parameter estimation problem. The key idea behind our methodology is to attempt the joint recovery of the solution, the sources along with the unknown parameters, thereby using the underlying partial differential equation as a constraint that couples multiple unknown functional parameters, leading to more efficient use of the limited information in the measurements. We present various numerical experiments, using different types of measurements that model practical engineering systems, to show that our proposed method is indeed successful and robust to additional noise in the measurements.

Keywords Source inversion, physics-informed neural networks, atmospheric science, joint recovery.

1 Introduction

Physics-informed Neural Networks (PINNs) [1] have been presented in the literature as a promising deep learning approach to solve partial differential equation (PDE) problems that incorporates the PDE as a constraint, allowing for the unified solution of forward and inverse problems [2, 1, 3]. One of the advantages of using PINNs is their flexibility in terms of their mathematical formulation and numerical implementation [1]. PINNs have also been successfully applied to solve high-dimensional PDEs in several application domains [4, 5].

The field of atmospheric dispersion modeling is concerned with the modeling of the dynamic behavior of pollutants in the atmosphere, often based on an Advection Diffusion Equation (ADE) [6]. A lot of research has been focused on

developing forward models for simulating the dispersion of pollutants by using physics and empirical data to build models for various parameters in ADE that dictate the advection and diffusion processes [7]. At the same time, one of the core problems in environmental modeling is the task of estimating sources of emissions which amounts to a source inversion problem for the ADE. However, lack of knowledge or presence of uncertainties in the ADE model parameters often amount to severe ill-posedness beyond those of standard source inversion problems. Adding to this the fact that data for source inversion is often quite noisy and scarce leads to an extremely challenging inverse problem. Motivated by PINNs’ capacity to seamlessly integrate data with PDE constraints [1], in this work, we develop an all-at-once approach using PINNs to simultaneously invert for sources and estimate unknown parameters of an ADE. Broadly speaking, our proposed method takes the following abstract form

$$\text{minimize}_{u,\gamma,f} \text{misfit}(u, \gamma, f, \mathbf{z}^*) \quad \text{subject to} \quad \mathcal{F}(u, \gamma) = f, \quad (1)$$

where \mathcal{F} denotes the differential operator defining ADE, u is the solution describing the concentration of the pollutant, γ denotes unknown parameters such as velocities and diffusion coefficients, f is the unknown source, and \mathbf{z}^* is the vector of measurements. We then discretize u, γ, f using neural networks and relax the PDE constraint with a Lagrange multiplier to obtain our PINN formulation, the details of this methodology are summarized in Section 2. This approach is successful because the PDE constraint restricts the manifold of possible solutions of the inverse problem which together with other prior constraints such as positivity of the source and the solution, and some of the other parameters in the model, enables us to solve the above optimization problem accurately.

1.1 Main contributions

To this end, our main contributions in this article can be summarized as follows:

- We introduce the joint optimization problem (1) and discretize and solve it using the PINN approach for solving source inversion problems with positivity constraints and unknown parameter fields γ .
- We derive a Neural Tangent Kernel (NTK) for our source inversion problem involving multiple neural networks and provide a theoretical justified training procedure for our joint optimization approach.
- We apply the training procedure mentioned above to solve various challenging 2D and 3D source inversion problems with sparse observations and constant or variable velocity and diffusion fields that are also assumed to be unknown and only informed by simple prior modeling assumptions.

1.2 Related Work

There have been many studies on source inversion problems in atmospheric dispersion modeling making use of several PDE solvers as well as both deterministic and Bayesian formulations [8, 9, 10, 11, 12, 13, 14, 15, 16, 17, 18, 19, 20]. In the Bayesian framework, emission sources can be modeled as unknown random variables given by appropriate prior distributions to be updated using the data via Bayes’ rule [11, 21, 13]. However, these works assume that the advection and diffusion parameters of the PDE are known, thereby obtaining a linear source inversion problem. The work [10] introduced a method for simultaneous source inversion and parameter estimation for a small number of scalar parameters and point sources using Gaussian process model emulators.

PINNs have been widely used for the solution of inverse problems in geosciences [22, 23, 24, 25, 26] as well as numerous engineering applications [27, 28, 29]. The idea of using PINNs for simultaneous learning of model parameters and the solution of forward or inverse problems has also been explored recently in [30] as well as the analogous Gaussian process formulations [31, 32], though these works consider the equation learning problem [33]; the problem of learning the governing PDE itself. Our work is inspired by these contributions and views inverse problems as a specific instance of equation learning where the unknown source as well as other model parameters take the role of unknown terms in the PDE at hand.

PINNs’ loss is usually unbalanced, since it combines different loss terms which can have different magnitude or convergence rates during the training process, which stands out as one of the challenges associated to PINNs’ training. To ensure a well-balanced loss function, the loss weights multiplying each loss terms have to be chosen carefully in a way that each of the loss terms have the same magnitude during the backpropagation of the loss by the gradient descent algorithm. Several approaches are presented in [34, 35, 36, 37, 38], as adaptive weighting methods to dynamically learn these weights during training. Among them, the Neural Tangent Kernel (NTK) introduced [39] has been used as an adaptive weighting method to describe the training dynamics and convergence of PINNs [38, 40, 41]. For these purposes, our work is presented as an extension of the NTK theory of PINNs initially developed for forward problems to a source inversion problem involving multiple neural networks.

1.3 Outline

The rest of the paper is organized as follows: In Section 2, we introduce some preliminaries on PINNs, our problem setup and the summary of our method and contributions; In Section 3, we present our theoretical analysis concerning the neural tangent kernel of PINNs in a source inversion problem with multiple neural networks; In Section 4, we

presents a description of our methodology; In Section 5 we present our numerical results on 2D and 3D ADE with constant and non-constant coefficients.

2 Preliminaries and problem setup

In this section, we recall some preliminary results and methodologies that form the basis of our proposed method followed by our problem setup in detail.

2.1 Physics-Informed Neural Networks (PINNs)

Numerical methods such as Finite Element Methods (FEM) and Finite Difference Methods (FDM), are widely used for solving inverse problems and they have well-established theoretical foundations [42, 43]. Recently, [1, 44, 33] introduced Physics-Informed Neural Networks (PINNs) as a promising tool to solve PDE problems by embedding the physics directly into the loss function of a neural net model, which is then minimized during the training process. This physics loss constrains the neural network not only to learn from the data, as is often the case using artificial neural networks, but also to learn while respecting the physics underneath. The attractive feature of PINNs is that it can seamlessly accommodate both forward and inverse PDE problems[1].

Considering a PDE problem written as

$$\begin{cases} \mathcal{F}[u(\mathbf{x}, t); \gamma] = f(\mathbf{x}, t), & \mathbf{x} \in \Omega, \quad t \in [0, T], \quad \Omega \subseteq \mathbb{R}^k, \quad T \in \mathbb{R} \\ u(\mathbf{x}, 0) = u_0(\mathbf{x}), & \mathbf{x} \in \Omega \\ \mathcal{B}[u(\mathbf{x}, t)] = g(\mathbf{x}, t), & \mathbf{x} \in \partial\Omega, \quad t \in [0, T] \end{cases} \quad (2)$$

with Ω an open bounded domain of \mathbb{R}^k ($k \geq 1$), \mathcal{F} the differential operator in $\Omega \times [0, T]$, \mathcal{B} the differential operator on $\partial\Omega$, u_0, g appropriate functions representing initial and boundary data, and γ the set of parameters in the differential equation.

2.1.1 Solving the forward problem with PINNs:

In this context, PINNs aim to approximate the solution u of (2), by parameterizing it as a neural net $u(\mathbf{x}, t; \boldsymbol{\theta})$ parameterized by a vector of weights $\boldsymbol{\theta}$, and then considering the training loss function:

$$\begin{aligned} \mathcal{L}(\boldsymbol{\theta}) &= \frac{\lambda_r}{N_r} \sum_{j=1}^{N_r} (\mathcal{F}[u(\mathbf{x}_r^j, t_r^j; \boldsymbol{\theta}); \gamma] - f(\mathbf{x}_r^j, t_r^j))^2 + \frac{\lambda_i}{N_i} \sum_{j=1}^{N_i} (u(\mathbf{x}_i^j, t_i^j; \boldsymbol{\theta}) - u_0(\mathbf{x}_i^j))^2 \\ &+ \frac{\lambda_b}{N_b} \sum_{j=1}^{N_b} (\mathcal{B}[u(\mathbf{x}_b^j, t_b^j; \boldsymbol{\theta})] - g(\mathbf{x}_b^j, t_b^j))^2, \end{aligned}$$

with $\lambda_r \in \mathbb{R}^+$, $\lambda_i \in \mathbb{R}^+$, $\lambda_b \in \mathbb{R}^+$ representing the weights multiplying the PDE residual, the initial data misfit, and the boundary data misfit, respectively. The $\{\mathbf{x}_r^j, t_r^j\}_{j=1}^{N_r}$, $\{\mathbf{x}_i^j, t_i^j\}_{j=1}^{N_i}$, $\{\mathbf{x}_b^j, t_b^j\}_{j=1}^{N_b}$ denote the sets of collocation points in the interior, initial condition, and boundary of the domain of the PDE, used to evaluate the pertinent residuals, constituting a penalty method for solving the PDE. This loss function is then minimized using gradient-based algorithms, typically the stochastic gradient descent algorithm, in order to find the optimal neural network parameters $\boldsymbol{\theta}^*$.

2.1.2 Solving source inversion with PINNs:

The variational nature of PINNs allows us to solve inverse problems in a very similar manner to the forward problem. More precisely, multiple neural nets can be employed to represent the solution u , as well as the source term f , and other unknown parameters γ of (2) from noisy data \mathbf{z}^* [13, 45, 44]. Therefore, the total loss being minimized takes the form:

$$\begin{aligned} \mathcal{L}(\boldsymbol{\theta}_u, \boldsymbol{\theta}_f, \boldsymbol{\theta}_\gamma) &= \frac{\lambda_r}{N_r} \sum_{j=1}^{N_r} (\mathcal{F}[u(\mathbf{x}_r^j, t_r^j; \boldsymbol{\theta}_u); \boldsymbol{\theta}_\gamma] - f(\mathbf{x}_r^j, t_r^j; \boldsymbol{\theta}_f))^2 + \frac{\lambda_z}{N_z} \sum_{j=1}^{N_z} (\tau_j(u(\cdot; \boldsymbol{\theta}_u)) - z_j^*)^2 \\ &+ \frac{\lambda_i}{N_i} \sum_{j=1}^{N_i} (u(\mathbf{x}_i^j, t_i^j; \boldsymbol{\theta}_u) - u_0(\mathbf{x}_i^j))^2 + \frac{\lambda_b}{N_b} \sum_{j=1}^{N_b} (\mathcal{B}[u(\mathbf{x}_b^j, t_b^j; \boldsymbol{\theta}_u)] - g(\mathbf{x}_b^j, t_b^j))^2 \end{aligned}$$

where we added the new weight $\lambda_z \in \mathbb{R}^+$, for the data misfit term. The data loss on the boundary data can also be added in the loss if the boundary data are available. The training process consists in finding the optimal neural network parameters $\{\boldsymbol{\theta}_u^*, \boldsymbol{\theta}_f^*, \boldsymbol{\theta}_\gamma^*\}$.

2.2 Our problem Setup

Let Ω be an open bounded domain in \mathbb{R}^k ($k \leq 3$) and fix $T > 0$ and consider the ADE:

$$\begin{cases} u_t(\mathbf{x}, t) + \nabla \cdot (V(\mathbf{x}, t)u(\mathbf{x}, t) - D(\mathbf{x}, t)\nabla u(\mathbf{x}, t)) = f(\mathbf{x}, t), & t \in [0, T], \quad \mathbf{x} \in \Omega \\ u(\mathbf{x}, 0) = g(\mathbf{x}, t) & \mathbf{x} \in \Omega \\ \mathcal{B}(u)(\mathbf{x}, t) = h(\mathbf{x}, t), & t \in [0, T], \quad \mathbf{x} \in \partial\Omega, \end{cases} \quad (3)$$

where $g : \Omega \rightarrow \mathbb{R}$ and $h : \Omega \times [0, T] \rightarrow \mathbb{R}$ are known continuous functions describing the boundary and initial data, $V : \Omega \times [0, T] \rightarrow \mathbb{R}^k$ is the advection/velocity field, $D : \Omega \times [0, T] \rightarrow \mathbb{R}_{\geq 0}$ is the diffusion coefficient, $f : \Omega \times [0, T] \rightarrow \mathbb{R}$ is the source term, and $\mathcal{B} : \partial\Omega \times [0, T] \rightarrow \mathbb{R}$ is an appropriate boundary operator. We consider the following setting:

- We have few noisy observations of the solution u of (3) with additive Gaussian noise:

$$z_i^* = \tau_i(u) + \varepsilon_i, \quad \varepsilon_i \sim \mathcal{N}(0, \sigma_i^2), \quad \sigma_i \in \mathbb{R}, \quad i = 1, \dots, N_z, \quad (4)$$

where the τ_i are bounded and linear operators that model our measurements and ε_i represents the noise.

- The source function f , the solution u of (3) and the parameters V and D are unknown and we aim to estimate them.

We now parameterize the solution u , the velocity V , the diffusion D and source term f as neural nets, with slight abuse of notation we write $u(\mathbf{x}, t; \boldsymbol{\theta}_u)$, $V(\mathbf{x}, t; \boldsymbol{\theta}_v)$, $D(\mathbf{x}, t; \boldsymbol{\theta}_d)$ and $f(\mathbf{x}; \boldsymbol{\theta}_f)$ to denote these neural nets with $\boldsymbol{\theta}$'s denoting the weights and biases of the pertinent networks. For problems where the velocity field V and the diffusion D are constant we simply consider them as parameters for the solution, i.e., within the vector $\boldsymbol{\theta}_u$. We then proceed to simultaneously train our neural networks by formulating the following PINN loss:

$$\mathcal{L}(\boldsymbol{\Theta}) = \underbrace{\lambda_r \mathcal{L}_r(\boldsymbol{\Theta})}_{\text{PDE residual}} + \underbrace{\lambda_b \mathcal{L}_b(\boldsymbol{\theta}_u)}_{\text{Boundary loss}} + \underbrace{\lambda_z \mathcal{L}_z(\boldsymbol{\theta}_u)}_{\text{Data loss}}, \quad \boldsymbol{\Theta} = \{\boldsymbol{\theta}_u, \boldsymbol{\theta}_v, \boldsymbol{\theta}_d, \boldsymbol{\theta}_f\} \quad (5)$$

where \mathcal{L}_r , \mathcal{L}_b and \mathcal{L}_z denote the residual, boundary, and data losses, respectively:

$$\begin{aligned} \mathcal{L}_r(\boldsymbol{\Theta}) &= \frac{1}{N_r} \sum_{i=1}^{N_r} (\mathcal{F}[u(\mathbf{x}_r^i, t_r^i; \boldsymbol{\theta}_u); \boldsymbol{\theta}_v; \boldsymbol{\theta}_d] - f(\mathbf{x}_r^i, t_r^i; \boldsymbol{\theta}_f))^2 \\ \mathcal{L}_b(\boldsymbol{\theta}_u) &= \frac{1}{N_b} \sum_{i=1}^{N_b} (\mathcal{B}[u(\mathbf{x}_b^i, t_b^i; \boldsymbol{\theta}_u)] - h(\mathbf{x}_b^i, t_b^i))^2 \\ \mathcal{L}_z(\boldsymbol{\theta}_u) &= \frac{1}{N_z} \sum_{i=1}^{N_z} (\tau_i[u(\cdot, \cdot; \boldsymbol{\theta}_u)] - z_i^*)^2 \end{aligned}$$

where we defined the differential operator $\mathcal{F}[u(\cdot; \boldsymbol{\theta}_u); \boldsymbol{\theta}_v; \boldsymbol{\theta}_d] := u_t(\cdot; \boldsymbol{\theta}_u) + \nabla \cdot (V(\cdot; \boldsymbol{\theta}_v)u(\cdot; \boldsymbol{\theta}_u) - D(\cdot; \boldsymbol{\theta}_d)\nabla u(\cdot; \boldsymbol{\theta}_u))$. Given that PINNs loss is usually unbalanced (loss components do not have the same magnitude), therefore, during the training process, the weights $\lambda_b, \lambda_r, \lambda_z$ are adaptively learned following the neural tangent kernel theory (NTK) introduced in [38]. As the NTK theory developed in the literature has mostly been focused on forward problems of PINNs, in this work, we extend the proposed weighted adaptive method to our source inversion problem, involving more than one neural network.

3 The neural tangent kernel of PINNs for our source inversion problem

In this section, we extend the NTK theory of PINNs for forward problems to a source inversion problem with parameter estimation based on the ADE (3). The derived NTK is a combined neural tangent kernel matrix of two separate neural networks, one for the source function f and the second for the solution u . In the case of unknown non-constant velocity and diffusion coefficients, the theory remains the same and will simply be extended to a combination of four NTK corresponding to their respective neural networks. Thus, to keep the notation simple we only present our results for the two network case.

Consider a gradient flow for our PINN loss:

$$\frac{d\boldsymbol{\Theta}(s)}{ds} = -\nabla_{\boldsymbol{\Theta}} \mathcal{L}(\boldsymbol{\Theta}), \quad \text{with } \boldsymbol{\Theta}(s) = \{\boldsymbol{\theta}_u(s), \boldsymbol{\theta}_f(s), \gamma(s)\}, \quad (6)$$

where $s \geq 0$ is a time parameter that models the flow of our gradient descent algorithm. The following lemma is our main theoretical contribution, the proof of which is summarized in Appendix A. This lemma presents the mathematical formulation of the NTK of PINNs in a source inversion problem on the ADE when V, D are constants. It gives a mathematical description at every iteration steps of the evolution of each term in the loss function $\mathcal{L}(\boldsymbol{\Theta})$ when back-propagated by gradient descent.

Lemma 1 Consider two neural networks $u(\mathbf{x}, t, \boldsymbol{\theta}_u)$ and $f(\mathbf{x}, t, \boldsymbol{\theta}_f)$ to approximate the solution u and the source function f , respectively and the gradient flow (6). Then along the path of this flow it holds that

$$\begin{bmatrix} \frac{d\mathcal{L}_r(\boldsymbol{\Theta}(s))}{ds} \\ \frac{d\mathcal{L}_b(\boldsymbol{\theta}_u(s))}{ds} \\ \frac{d\mathcal{L}_z(\boldsymbol{\theta}_u(s))}{ds} \end{bmatrix} = -\mathbf{K}(s) \begin{bmatrix} \mathcal{F}[u(\mathbf{x}_r, t_r; \boldsymbol{\theta}_u(s)); \gamma(s)] - f(\mathbf{x}_r, t_r, \boldsymbol{\theta}_f(s)) \\ \mathcal{B}[u(\mathbf{x}_b, t_b; \boldsymbol{\theta}_u(s))] - h(\mathbf{x}_b, t_b) \\ \tau[u(\mathbf{x}_z, t_z; \boldsymbol{\theta}_u(s))] - \mathbf{z}^* \end{bmatrix} \quad (7)$$

where

$$\mathbf{K}(s) = \begin{bmatrix} \mathbf{K}_{rr}(s) & \mathbf{K}_{rb}(s) & \mathbf{K}_{rz}(s) \\ \mathbf{K}_{br}(s) & \mathbf{K}_{bb}(s) & \mathbf{K}_{bz}(s) \\ \mathbf{K}_{zr}(s) & \mathbf{K}_{zb}(s) & \mathbf{K}_{zz}(s) \end{bmatrix} \begin{bmatrix} \frac{2\lambda_r}{N_r} \\ \frac{2\lambda_b}{N_b} \\ \frac{2\lambda_z}{N_z} \end{bmatrix} \quad (8)$$

and

$$\left\{ \begin{array}{l} (\mathbf{K}_{rr})_{ij}(s) = \left\langle \left(\frac{\frac{d\mathcal{F}[u(\mathbf{x}_r^i, t_r^i; \boldsymbol{\theta}_u(s)); \gamma(s)]}{d\boldsymbol{\theta}_u}}{df(\mathbf{x}_r^i, t_r^i, \boldsymbol{\theta}_f(s))} \right), \left(\frac{\frac{d\mathcal{F}[u(\mathbf{x}_r^j, t_r^j; \boldsymbol{\theta}_u(s)); \gamma(s)]}{d\boldsymbol{\theta}_u}}{df(\mathbf{x}_r^j, t_r^j, \boldsymbol{\theta}_f(s))} \right) \right\rangle \\ = (J_{rr}^{\boldsymbol{\theta}_u}(s))(J_{rr}^{\boldsymbol{\theta}_u}(s))^T + (J_{rr}^{\boldsymbol{\theta}_f}(s))(J_{rr}^{\boldsymbol{\theta}_f}(s))^T + (J_{rr}^{\gamma}(s))(J_{rr}^{\gamma}(s))^T \\ (\mathbf{K}_{bb})_{ij}(s) = \left\langle \frac{d\mathcal{B}[u(\mathbf{x}_b^i, t_b^i; \boldsymbol{\theta}_u(s))]}{d\boldsymbol{\theta}_u}, \frac{d\mathcal{B}[u(\mathbf{x}_b^j, t_b^j; \boldsymbol{\theta}_u(s))]}{d\boldsymbol{\theta}_u} \right\rangle \\ (\mathbf{K}_{zz})_{ij}(s) = \left\langle \frac{d\tau_i[u(\mathbf{x}_z^i, t_z^i; \boldsymbol{\theta}_u(s))]}{d\boldsymbol{\theta}_u}, \frac{d\tau_j[u(\mathbf{x}_z^j, t_z^j; \boldsymbol{\theta}_u(s))]}{d\boldsymbol{\theta}_u} \right\rangle \\ (\mathbf{K}_{br})_{ij}(s) = \left\langle \frac{d\mathcal{B}[u(\mathbf{x}_b^i, t_b^i; \boldsymbol{\theta}_u(s))]}{d\boldsymbol{\theta}_u}, \frac{d(\mathcal{F}[u(\mathbf{x}_r^j, t_r^j; \boldsymbol{\theta}_u(s)); \gamma(s)] - f(\mathbf{x}_r^j, t_r^j, \boldsymbol{\theta}_f(s)))}{d\boldsymbol{\theta}_u} \right\rangle \\ (\mathbf{K}_{zr})_{ij}(s) = \left\langle \frac{d\tau_i[u(\mathbf{x}_z^i, t_z^i; \boldsymbol{\theta}_u(s))]}{d\boldsymbol{\theta}_u}, \frac{d(\mathcal{F}[u(\mathbf{x}_r^j, t_r^j; \boldsymbol{\theta}_u(s)); \gamma(s)] - f(\mathbf{x}_r^j, t_r^j, \boldsymbol{\theta}_f(s)))}{d\boldsymbol{\theta}_u} \right\rangle \\ (\mathbf{K}_{zb})_{ij}(s) = \left\langle \frac{d\tau_i[u(\mathbf{x}_z^i, t_z^i; \boldsymbol{\theta}_u(s))]}{d\boldsymbol{\theta}_u}, \frac{d\mathcal{B}[u(\mathbf{x}_b^j, t_b^j; \boldsymbol{\theta}_u(s))]}{d\boldsymbol{\theta}_u} \right\rangle \end{array} \right.$$

with $\langle \cdot, \cdot \rangle$ representing the Euclidean inner product in the neural network parameters space. Here we have $\mathbf{K}_{rr} \in \mathbb{R}^{N_r \times N_r}$, $\mathbf{K}_{bb} \in \mathbb{R}^{N_b \times N_b}$, $\mathbf{K}_{zz} \in \mathbb{R}^{N_z \times N_z}$, $\mathbf{K}_{br} \in \mathbb{R}^{N_b \times N_r}$, $\mathbf{K}_{br} = (\mathbf{K}_{rb})^T$, $\mathbf{K}_{zr} \in \mathbb{R}^{N_z \times N_r}$, $\mathbf{K}_{zr} = (\mathbf{K}_{rz})^T$, $\mathbf{K}_{zb} \in \mathbb{R}^{N_z \times N_b}$ and $\mathbf{K}_{zr} = (\mathbf{K}_{rz})^T$.

It has been shown in [38], The NTK $\mathbf{K}(s)$ is a positive semi-definite matrix and converges in probability to a deterministic kernel $\mathbf{K}^* \simeq \mathbf{K}(0)$ at initialization. Therefore, (7) becomes

$$\begin{bmatrix} \frac{d\mathcal{L}_r(\boldsymbol{\Theta}(s))}{ds} \\ \frac{d\mathcal{L}_b(\boldsymbol{\theta}_u(s))}{ds} \\ \frac{d\mathcal{L}_z(\boldsymbol{\theta}_u(s))}{ds} \end{bmatrix} \simeq -\mathbf{K}(0) \begin{bmatrix} \mathcal{F}[u(\mathbf{x}_r, t_r; \boldsymbol{\theta}_u(s)); \gamma(s)] - f(\mathbf{x}_r, t_r, \boldsymbol{\theta}_f(s)) \\ \mathcal{B}[u(\mathbf{x}_b, t_b; \boldsymbol{\theta}_u(s))] - h(\mathbf{x}_b, t_b) \\ \tau[u(\mathbf{x}_z, t_z; \boldsymbol{\theta}_u(s))] - \mathbf{z}^* \end{bmatrix}$$

which implies that

$$\mathbf{Q} \left(\begin{bmatrix} \frac{d\mathcal{L}_r(\boldsymbol{\Theta})}{ds} \\ \frac{d\mathcal{L}_b(\boldsymbol{\theta}_u)}{ds} \\ \frac{d\mathcal{L}_z(\boldsymbol{\theta}_u)}{ds} \end{bmatrix} - \begin{bmatrix} 0 \\ h(\mathbf{x}_b, t_b) \\ \mathbf{z}^* \end{bmatrix} \right) \simeq -e^{\Gamma t} \mathbf{Q} \begin{bmatrix} 0 \\ h(\mathbf{x}_b, t_b) \\ \mathbf{z}^* \end{bmatrix}$$

since $\mathbf{K}(0)$ is symmetric positive semi-definite, and can be written as $\mathbf{K}(0) = \mathbf{Q}^T \Gamma \mathbf{Q}$ where \mathbf{Q} is an orthogonal matrix [38]. This means that the residual, boundary and data loss terms in the objective converges at the rates $e^{-\alpha_r s}$, $e^{-\alpha_b s}$, $e^{-\alpha_z s}$ respectively, where $\alpha_r, \alpha_b, \alpha_z$ are the eigenvalues of $\mathbf{K}_{rr}, \mathbf{K}_{bb}$ and \mathbf{K}_{zz} .

Despite the NTK theory of PINNs being introduced already by in [38], we chose to present its theoretical derivation to a source inversion problem in order to give a detailed description of the training algorithm of the weighted adaptive method used in this work, from which all our numerical results presented in Section 5 rely on. We would like to also point out that weighted adaptive method based on NTK of PINNs have been less explored on inverse problems and source inversion problems with parameter estimation as compared to forward problems. To the best of our knowledge, this is the first time this adaptive method, is used to quantify the PINNs performance in a source inversion problem with parameter estimation.

4 Methodology

We now summarize our methodology for solving source inversion using PINNs and the NTK informed adaptation of weights in our objective. In our numerical experiments, we considered our noisy observations on the solution u inside the spacial domain Ω and we assume we have few noisy data of the solution at $\partial\Omega$. The amount of boundary data chosen is $\frac{\beta}{1000}$ ($\beta > 0$) times the total amount of boundary data. We have chosen β to be 11 in the 2D case with constants coefficients, and 1 in 2D and 3D case with variable coefficients. We used 4 separate neural networks to approximate the unknowns u , V , D and f in the most general version of our algorithm. At the early stage of the training the weights λ_r , λ_b , λ_z are initialized to 1 before being adaptively updated using the formula (9) as given in [38]:

$$\lambda_r = \frac{Tr(\mathbf{K}(s))}{Tr(\mathbf{K}_{rr}(s))}, \quad \lambda_b = \frac{Tr(\mathbf{K}(s))}{Tr(\mathbf{K}_{bb}(s))}, \quad \lambda_z = \frac{Tr(\mathbf{K}(s))}{Tr(\mathbf{K}_{zz}(s))}. \quad (9)$$

At this stage we use stochastic gradient descent. Once these weights are adapted and remain consistent, we fix their values and start the second phase of the training where L-BFGS is used to update the network parameters θ_u , θ_f , θ_d , θ_v . This process is summarized in Algorithm 1.

Algorithm 1 PINNs + NTK Training Algorithm for Source Inversion Problem

- 1: **Initialize** 4 separate feedforward neural networks $u(\mathbf{x}, t, \theta_u)$, $f(\mathbf{x}, t, \theta_f)$, $V((\mathbf{x}, t, \theta_v))$, $D(\mathbf{x}, t, \theta_d)$ (when V and D are variable coefficients) or initialize V and D to 1.0 when they are constants.
 - 2: **Initialize** $\lambda_r = \lambda_b = \lambda_z = 1$
 - 3: **Backpropagation** of $\mathcal{L}(\Theta)$ with ADAM and learning rate η
 - 4: **for** $j = 1$ to \max_{iter} **do**
 - 5: Compute the loss function $\mathcal{L}(\Theta)$ in (5)
 - 6: Compute the NTK \mathbf{K} in (8)
 - 7: $\theta_u^j \leftarrow \theta_u^{j-1} - \eta \nabla_{\theta_u} \mathcal{L}(\Theta)$
 - 8: $\theta_f^j \leftarrow \theta_f^{j-1} - \eta \nabla_{\theta_f} \mathcal{L}(\Theta)$
 - 9: $\theta_v^j \leftarrow \theta_v^{j-1} - \eta \nabla_{\theta_v} \mathcal{L}(\Theta)$
 - 10: $\theta_d^j \leftarrow \theta_d^{j-1} - \eta \nabla_{\theta_d} \mathcal{L}(\Theta)$
 - 11: Update the loss weights:

$$\lambda_r = \frac{Tr(\mathbf{K})}{Tr(\mathbf{K}_{rr})}, \quad \lambda_b = \frac{Tr(\mathbf{K})}{Tr(\mathbf{K}_{bb})}, \quad \lambda_z = \frac{Tr(\mathbf{K})}{Tr(\mathbf{K}_{zz})},$$
 - 12: **end for**
 - 13: **Update** Keep λ_r , λ_b , λ_z fixed and use L-BFGS to update network weights θ_u , θ_f , θ_v , θ_d
 - 14: **return** θ_u , θ_f , θ_v , θ_d
-

5 Numerical Results

In this section, we present our numerical results for various synthetic instances of the ADE in the 2D and 3D for both variable and constant velocity and diffusion fields. All experiments were performed using the TorchPhysics library on an NVIDIA RTX 5000 Ada Generation GPU.

5.1 2D-Advection-diffusion equation with constant coefficients

We consider the 2D Advection-diffusion equation (3) on $\Omega = [0, 1] \times [0, 1]$. We assume that the boundary of the domain is reflective to pollutants particles, therefore the boundary condition on (3) becomes a Neumann boundary condition $\nabla_n(u)(\mathbf{x}, t) = 0 \quad t \in [0, 1]$, $\mathbf{x} \in \partial\Omega$. We consider the initial condition $u(\mathbf{x}, 0) = 0 \quad \mathbf{x} \in \Omega$ and assume constant diffusion D and velocities coefficient V .

We assume that the emission source function is a mixture of two Gaussians:

$$f(x, y) = \exp\left(-\frac{(x - \mu_1)^2}{2l_1^2}\right) + \exp\left(-\frac{(y - \mu_2)^2}{2l_2^2}\right) \quad (10)$$

We first solved the above problem using Finite Element Method (FEM), with $V = (0.2, -0.2)$, $D = 0.01$, $\mu_1 = 0.25$, $\mu_2 = 0.75$, $l_1 = 0.06$ and $l_2 = 0.04$ to generate a ground truth solution. From the FEM solution, we derive two types of observation data that correspond to the following assumptions.

- (Pointwise Observations) The observations result from sensors taking direct time series measurements of the air pollutant concentration, that is in 4 we took $\tau_i(u) = u(\mathbf{x}_i, t_i)$ for a fixed location \mathbf{x}_i and time t_i .
- (Accumulative Observations) Observations result from sensors capturing average of air pollutants concentrations over a fixed time interval of length δ_t , i.e. $\tau_i(u) = \int_{t_i}^{t_i+\delta_t} u(\mathbf{x}_i, s) ds$.

5.1.1 Pointwise observations

We randomly choose 4 and 15 spatial locations at which we have noisy time series measurements of the FEM solution as shown in Figure 1. We have considered two separate neural networks $u(\mathbf{x}, t; \theta_u)$ with 3 hidden layers, 80 neurons per layer and $f(\mathbf{x}; \theta_f)$ with 3 hidden layers, 100 neurons per layer to approximate u and f respectively with both networks using tanh activation functions. We applied Algorithm 1 with 15000 ADAM optimizer steps and learning rate $\eta = 10^{-3}$ followed by 20000 iterations of L-BFGS with learning rate $\eta = 0.1$.

We observe in Figures 2 (see also Figures 15 and 16) that despite having only 4 pointwise measurements, our method is able to obtain acceptable estimates of the solution u and the source f at various noise levels. We also see that by increasing the number of observations to 15 points the recovery of both u and f improved as expected. We consistently observed that the solution u was recovered more accurately than f . This is natural due to the fact that we had access to direct observations of u .

We repeated our experiments 5 times by randomizing the noise and report our average recovered values of the velocities and the diffusion coefficient in Table 1. We observed that our method is generally capable of recovering these unknown parameters from the scarce data while giving good recoveries of u and f .

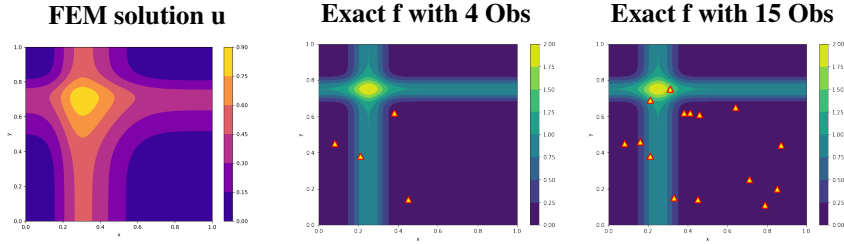


Figure 1: **Contour Plots of the FEM solution at $t = 1$ (left), Exact source function with 4 measurements locations(middle) and 15 measurement locations (right), with the the selected measurements locations represented by the triangles.**

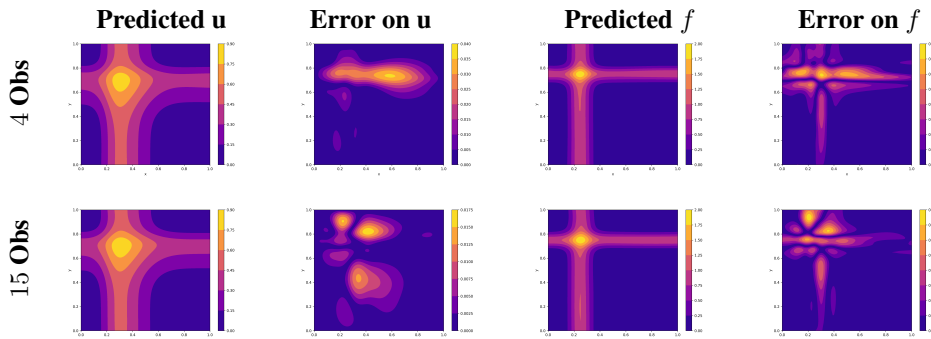


Figure 2: **Prediction and absolute error of u at $t = 1$ and f , with 1% of noise.**

We observe from the Figures 3 and 4 in a context of an inverse problem, at initialization, the residual dominates the data losses while we observe the opposite when solving the ADE in the forward context. In addition to the losses on the residual, initial and boundary condition in the forward problem, we also added a data loss $\mathcal{L}_z(\theta_u)$. Despite having 15 observations of u in the forward case with up to 80000 iterations, we observe a very slow convergence of the residual as well as the data misfit term while their convergence is faster in the inverse context. This simply means that when solving the forward problem the algorithm first learns a solution that fits the initial and boundary condition before the PDE residual is reduced. In the inverse problem case, the solution matching the PDE is learned first before it is constrained

4 Obs	V_x		V_y		D	
Noise	Predicted	Relative error	Predicted	Relative error	Predicted	Relative error
1%	0.20074	0.37%	-0.2014	0.7%	0.00944	5.6%
5%	0.20151	0.75%	-0.20174	0.87%	0.00933	6.7%
10%	0.2038	1.9%	-0.2058	2.9	0.00917	8.3%
15 Obs	V_x		V_y		D	
Noise	Predicted	Relative error	Predicted	Relative error	Predicted	Relative error
1%	0.19781	1.1%	-0.19782	1.1%	0.00974	2.6%
5%	0.1962	1.94%	-0.19496	2.58%	0.0096	4.16 %
10%	0.19593	2%	-0.19313	3.55%	0.00957	4.49%

Table 1: Predicted values of the velocities and diffusion coefficients with their relative error, assuming 4 and 15 observations locations with an identity observation operator

to fit the available data. We view this empirical observation as evidence that the NTK adaptation approach is better suited for inverse problems as it was also observed by [38].

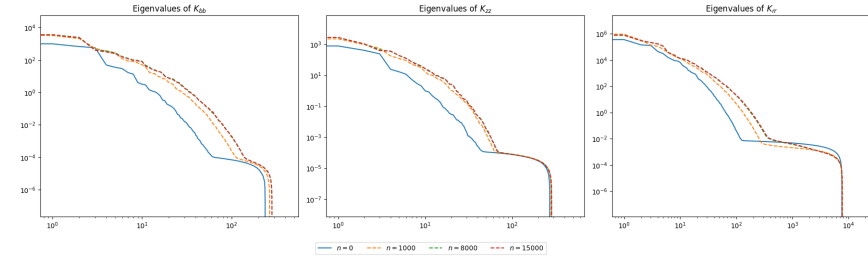


Figure 3: Eigenvalues in a source inversion problem of K_{bb} , K_{zz} , K_{rr} vs their index, with 15 observations on u .

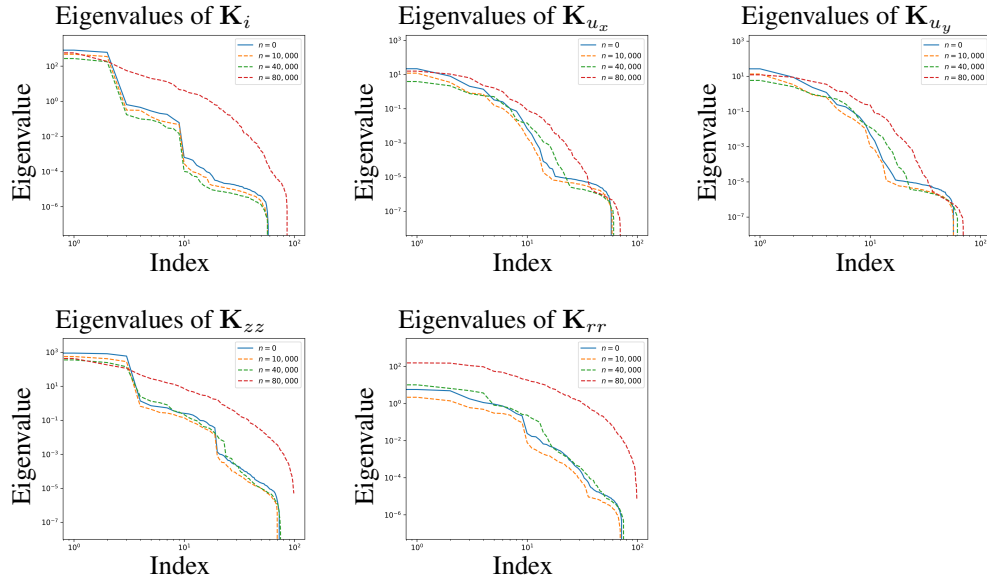


Figure 4: Eigenvalues in a forward context of K_i , K_{u_x} , K_{u_y} , K_{zz} , K_{rr} vs their index with n representing the number of iterations.

5.1.2 Accumulative Observations

In this scenario, we assume that at each measurements locations, we have the average of the solution u over a fixed time interval of length $\delta t = 30$. One can think of a scenario where in a day, the sensors capture air pollutants concentration

after 30 seconds, each concentration values representing the average of concentration over 30 seconds. We have conducted the same experiments as in the previous scenario, with 4 and 15 measurements locations, using the same architectures for the neural networks on u and f , with positivity constraints imposed on D and f . The PINNs' model performance has slightly decreased in this case, compared to the scenario with pointwise observations, since the amount of measurement data has reduced. We observe from the Figures 5 and 18 that, our method produces good approximations of the solution, the source function and the PDE parameters despite the limited number of measurements data, the high ill-posedness of the problem as well as the noise level variation. However, we notice from the Table 2 a very poor approximation of the diffusion coefficient with 4 observations at 10% of noise. This is due to the insufficient number of measurements data necessary for it approximation, suggesting that in this case the model might be trying to approximate D from the noise since the chosen measurements locations are not well spatially distributed for a good coverage of the spatial domain. An increase of the number of measurements locations makes the model to give a better approximation of D as expected, and as shown in Table 2.

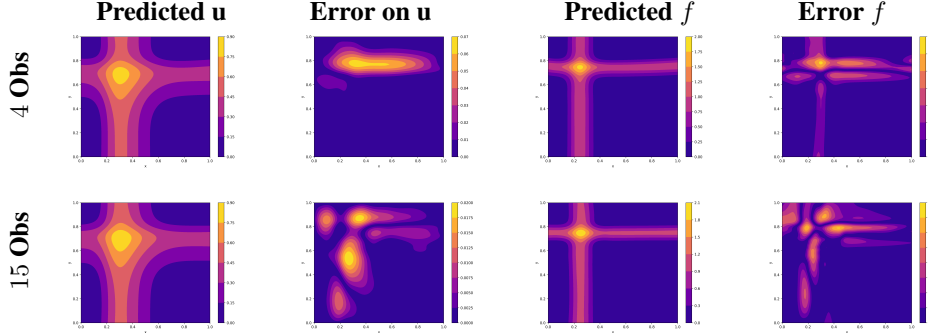


Figure 5: Prediction and error of u and f with 1% of noise and average observation operator over $\delta t = 30$.

4 Obs	Vx		Vy		D	
Noise	Predicted	Relative error	Predicted	Relative error	Predicted	Relative error
1%	0.19912	0.44%	-0.20525	2.62%	0.008643	13.57%
5%	0.19469	2.65%	-0.15938	20.31%	0.00538	46.2%
10%	0.18404	7.98%	-0.23356	16.78%	0.0021	79%
15 Obs	Vx		Vy		D	
Noise	Predicted	Relative error	Predicted	Relative error	Predicted	Relative error
1%	0.19713	1.44%	-0.19977	0.11%	0.009849	1.53%
5%	0.19009	4.95%	-0.1942522	2.87%	0.007424	25.76%
10%	0.18095	9.52%	-0.20362	1.81%	0.005604	43.96%

Table 2: Predicted values of the velocities and diffusion coefficients with their relative error, assuming 4 and 15 observations locations with an average observation operator on u over time intervals of length $\delta t=30$.

5.2 2D-ADE with Non Constants Velocity and Diffusion Coefficients

In this section we consider the same 2D advection diffusion equation (3), with a time-dependent velocity vector, and a time-independent diffusion coefficient. We consider the same source function as in (10), and we solve the problem using Finite Element Method with $V(t) = (V_1(t), V_2(t)) = (0.2 + 0.1 \sin(2\pi t), -0.2 - 0.1 \cos(2\pi t))$ and $D(x, y) = 0.1(1 + \sin(\pi x) \cos(\pi y)/2)$. We randomly select 30 locations at which we assume we have noisy observations \mathbf{z}^* and velocity data. We used 4 separate Neural Networks $u(\mathbf{x}, t, \theta_u)$, $f(\mathbf{x}, \theta_f)$, $V(t, \theta_v)$, $D(\mathbf{x}, \theta_d)$ to approximate u , f , V and D respectively. In addition to the PDE constraint, we also add a positive constraint on the source f in the PINN model, which lead to following constrained minimization problem:

$$\min_{\Theta} \mathcal{L}(\Theta) \quad \text{s.t.} \quad f(\mathbf{x}, t, \theta_f) \geq 0, \quad \forall (\mathbf{x}, t) \in \Omega \times [0, T] \quad (11)$$

with $\Theta = \{\theta_u, \theta_v, \theta_d, \theta_f\}$ and $\mathcal{L}(\Theta)$ given in (5). Once again, we simultaneously trained these neural networks using the weighted adaptive method based on NTK for PINNs while using 20000 iterations on ADAM (with learning rate 0.001) followed by 30000 iterations with L-BFGS optimizer with learning rate 0.1 .

Although we have a limited number of measurements, the weighted adaptive method on PINNs accurately approximates the velocity, and the solution u as we can observe on Figure 6, 9. We observe good approximation of the diffusion coefficients with a Mean Absolute Error (MAE) of $6.6017e - 03$, a relative $L2$ error of $8.7316e - 02$ and larger error values on the absolute point wise error of the diffusion Figure7, because no boundary on initial condition on D were given to the model. This does not influence the approximation of the source function since, on the Figure 10, the absolute error on f is larger at the locations at which the approximation error of the solution u also yields the highest absolute error value. The small amount of observations on u might not cover enough the spatial domain, making it hard for the PINNs to capture correctly the shape of the diffusion component.

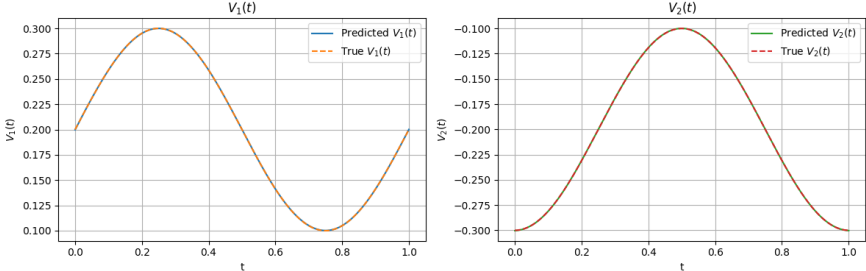


Figure 6: Plot of predicted vs exact velocity component over time

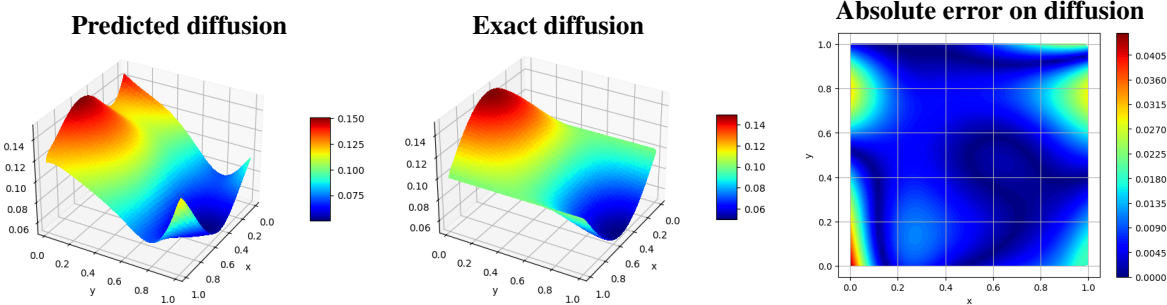


Figure 7: *Left*: surface plots of predicted diffusion. *Middle*: exact diffusion *Right*: Contour plot of the absolute error on the diffusion.

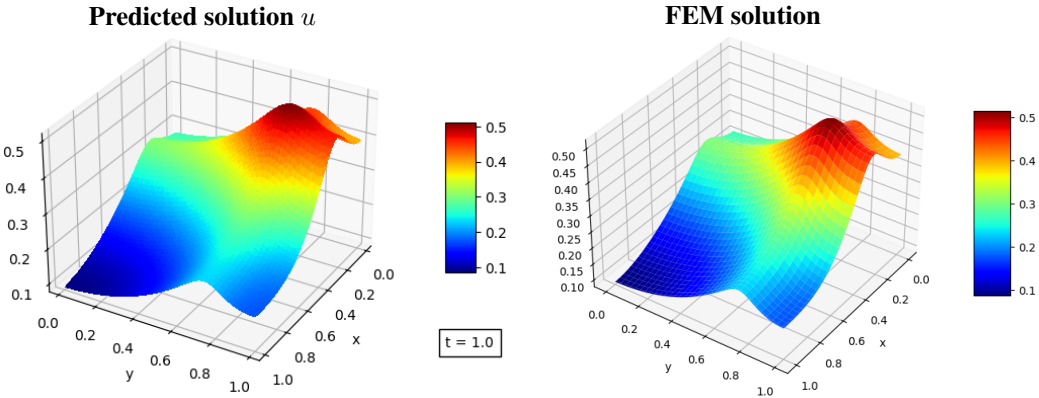


Figure 8: Surface Plots of the Predicted vs FEM Solution u at $t = 1.0$

5.3 3D Advection-Diffusion Equation with Height-Dependent Velocity and Diffusion Parameters

We dive into a higher-dimensional case where we consider a 3D spatial domain. In this experimental case, we consider a 3D ADE on a unit cube $\Omega = [0, 1]^3$ with a Neumann boundary condition at the top boundary layer $z = 1$ (a reflective boundary layer at $z = 1$) and a Dirichlet condition at the boundary of the domain except the top boundary $z = 1$.

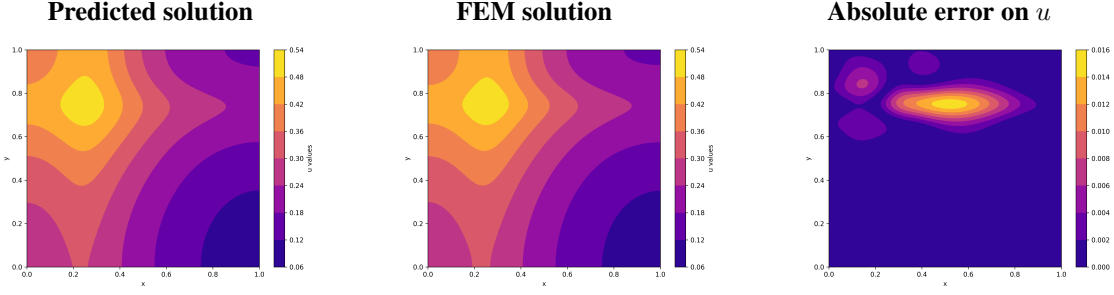


Figure 9: Contour Plots of the Predicted(left) vs FEM Solution(middle) and the absolute error(right) of u at $t = 1$.

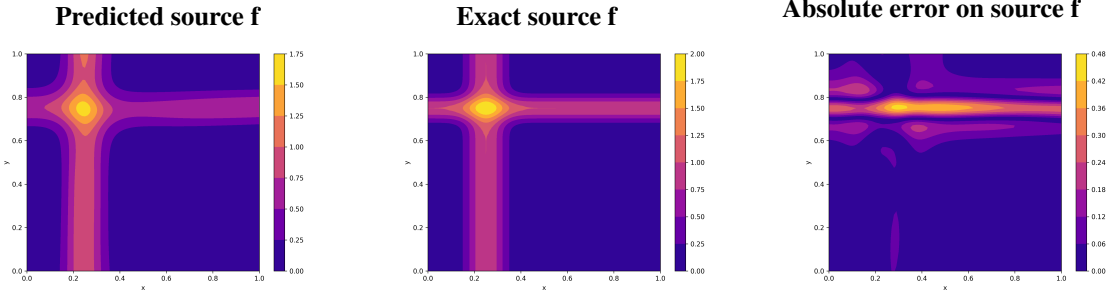


Figure 10: Contour Plots of the Predicted (left) vs Exact (middle) Source function with the absolute error(right).

Therefore, we have the initial and boundary conditions $u(\mathbf{x}, 0) = 0 \quad \mathbf{x} \in \Omega$, $D_z \frac{\partial u}{\partial z}(\mathbf{x}, t) = 0$, at $z = 1$, and $u(\mathbf{x}, t) = 0$ for $\mathbf{x} \in \partial\Omega \setminus \{z = 1\}$ respectively. We assume that the wind speed V is time and height dependent, that is $V(z, t) = (V_1(z, t), V_2(z, t), V_3)$ with $V_3 = V_{set}$ the setting velocity given by the Stokes law [46, 47, 48] as $V_{set} = \frac{\rho g d^2}{18\mu}$ where $\rho = 1500[kg/m^3]$, $d = 2e^{-6}[m]$, $g = 9.8[m/s^2]$, $\mu = 1.8 \times 10^{-5}[kg/ms]$ represent the air pollutants density, the air pollutants diameter, the gravitational acceleration and the viscosity of air respectively. We also assume that V_1 and V_2 are derived from the power law correlation [49] at the reference altitude of $z = 0.5$, with the reference velocity denoted as V_{ref} . Therefore, we have $V_1(z, t) = \left(\frac{z}{0.5}\right)^\alpha V_{ref}$ with $V_{ref} = 0.8(1 + \sin(2\pi t))$ and $V_2(z, t) = -V_1(z, t)$. We assume $\alpha = 0.4$, which corresponds to a rough surface domain. We assume that we have 3 different locations of emission sources $S = \{(0.25, 0.75, 0.5), (0.52, 0.8, 0.8), (0.6, 0.28, 0.3)\}$ with their respective emission rate $\eta_1 = 5, \eta_2 = 3, \eta_3 = 1$. The exact source function is the sum of the Gaussian kernel functions at those locations with the respective standard deviation $\sigma_1 = 0.2, \sigma_2 = 0.06, \sigma_3 = 0.08$ and consequently, f is written as

$$f(x, y, z) = \sum_{i=1}^3 \eta_i \exp\left(-\frac{((x - x_i^i)^2 + (y - y_i^i)^2 + (z - z_i^i)^2)}{2\sigma_i^2}\right) \quad \text{for } (x_i, y_i, z_i) \in S$$

We assume the the first two components of the diffusion coefficient to be isotropic in the XZ-plane and the third component height dependent only with a boundary layer $H = 1$ i.e $D(x, z) = (D_1(x, z), D_2(x, z), D_3(z)) = (0.2 + x^2(z/0.5)^\alpha, 0.2 + x^2(z/0.5)^\alpha, 0.2 + 0.1(\frac{z}{H})^\alpha)$. We also assume we have 30 measurements locations at which we have noisy data and noisy wind speed data \hat{V} at those locations. Therefore, the loss function is similar to (5) with $\mathbf{x} = (x, y, z)$. Under the above-mentioned assumptions, we randomly choose 30 measurements locations and initialize the neural networks $u(\mathbf{x}, t, \theta_u), f(\mathbf{x}, \theta_f), V(t, \theta_v), D(\mathbf{x}, \theta_d)$ with $[4, 80, 80, 80, 80, 1]$, $[3, 100, 100, 100, 1]$, $[2, 80, 80, 80, 60, 60]$, $[2, 80, 80, 80, 80, 80, 1]$ respectively. The training process of these neural networks is spited into three phases:

Pretraining phase: we first train the model with 10000 ADAM optimizer while minimizing the data losses of (5), that is,

$$\frac{1}{N_b} \sum_{i=1}^{N_b} (\mathcal{B}[u(\mathbf{x}_b^i, t_b^i; \theta_u)] - h(\mathbf{x}_b^i, t_b^i))^2 + \frac{1}{N_z} \sum_{i=1}^{N_z} (\tau_i[u(\mathbf{x}_z^i, t_z^i; \theta_u)] - \mathbf{z}_i^*)^2 + \frac{1}{N_v} \sum_{i=1}^{N_v} (v(t_v^i; \theta_v)] - V^*(t_v^i))^2$$

The loss weights are not updated in this phase.

Training phase while updating the loss weights: we train the PINN model with 20000 ADAM optimizer using the total loss (5). The neural networks parameters Θ , as well as the loss weights $\lambda_r, \lambda_b, \lambda_v$ and λ_z are being updated during

the training.

Fine tuning with L-BFGS: the third phase consists of updating Θ to minimize (5) using L-BFGS over 30000 iterations. We observe in the following numerical results that once again the PINNs model is able to achieve a good approximation on the velocity vector (Figure 11) with an absolute error of 0 almost everywhere in the domain except at the left boundary of the domain. This is because no initial or boundary conditions on the velocity have been imposed to the model and therefore, when $z = 0$ the model might be learning only from the noise, resulting in an approximation with higher error at $z = 0$. In addition, the model approximates $V_3 = 2.25e - 5$ with a higher amplitude compared to $2.893518518518519e - 07$ the exact value since the true value is extremely small. The model is still able to approximate well the solution u with a MAE of $2.4e - 2$ as we observe in Figure 13, achieving at the final time $t = 1.0$ an L2-error of $5.6e - 3$ and a relative error of $1e - 2$. The approximated source function, on the other hand, at the altitudes $z = 0.3$ and reference altitude $z = 0.5$ were well captured with slight low amplitude compared to the exact source function and this is be due to the ill-posedness. Furthermore, the PINN model gives a good approximation of diffusion in the xz -plane Figure 12, while we do not observe good performance in approximate diffusion in the z direction once again due to the ill-posedness of the problem and the limited number of measurements locations.

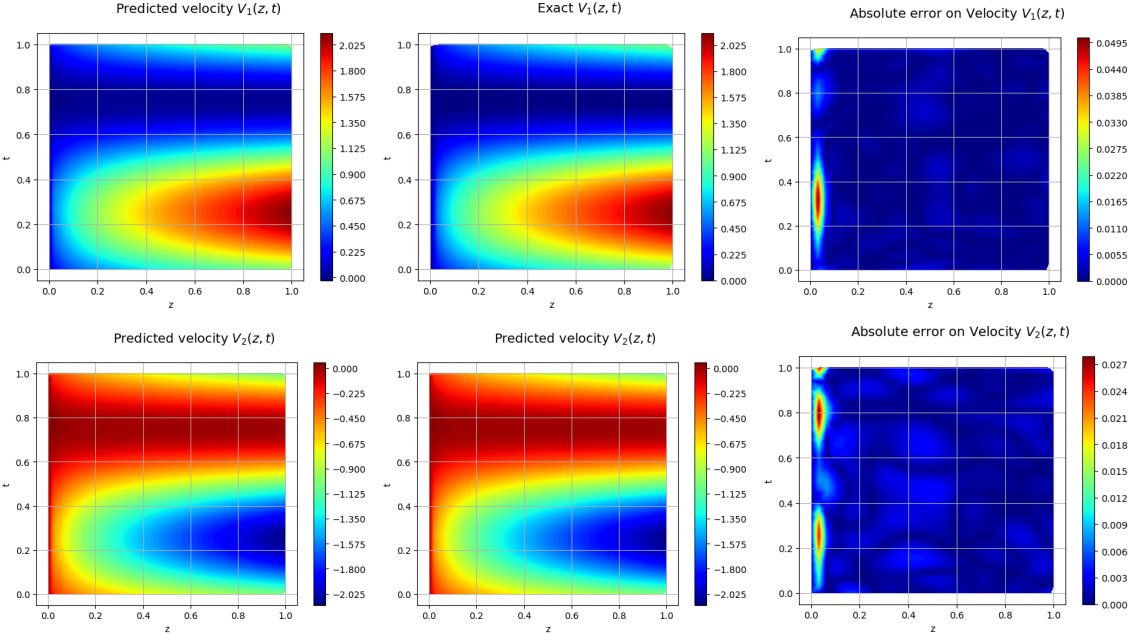


Figure 11: *Top row:* Contour plots of predicted (left), exact (middle) and absolute error (right) of the velocity function $V_1(z, t)$. *Bottom row:* Contour plots of predicted (left), exact (middle) and absolute error (right) of the velocity function $V_2(z, t)$.

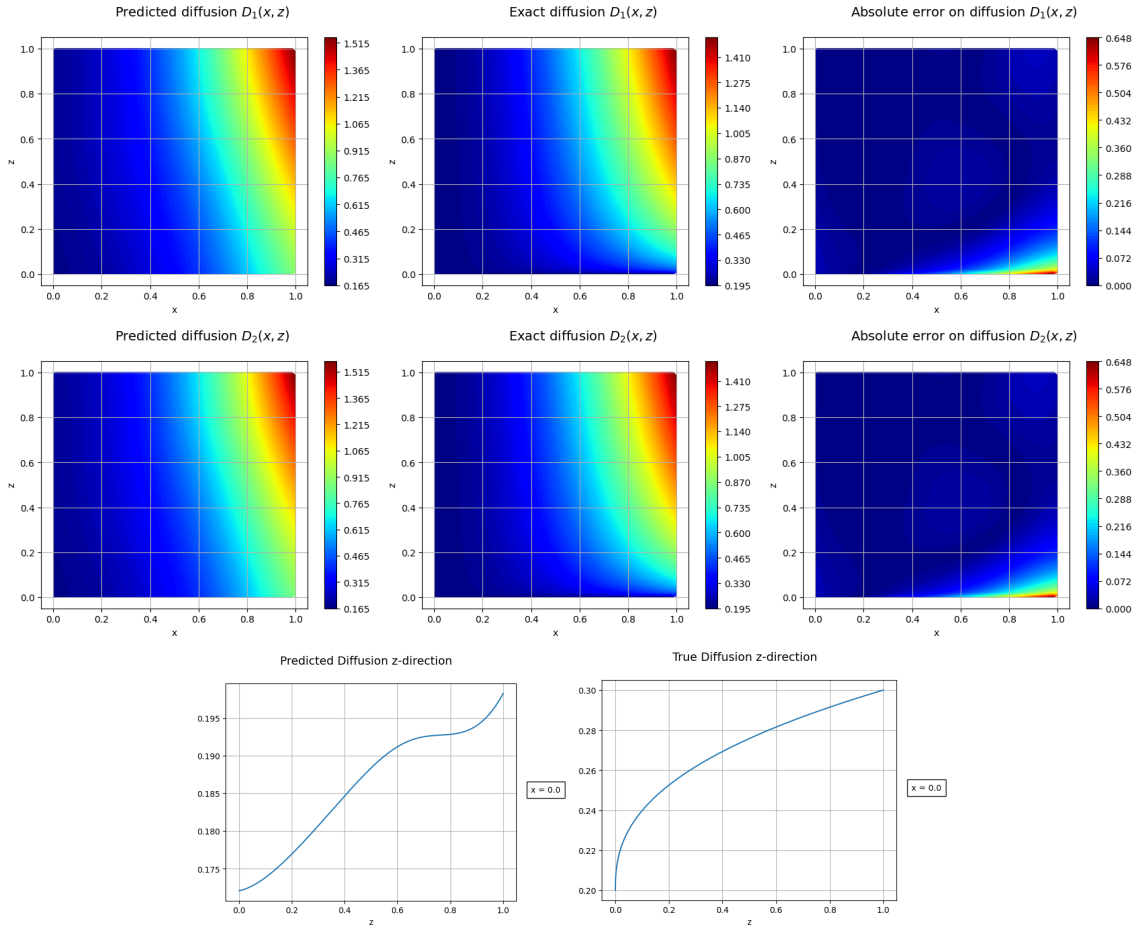


Figure 12: *Top and middle row: Contour plots of predicted (left), exact (middle) and absolute error (right) of the Diffusion functions $D_1(x, z)$ and $D_2(x, z)$ respectively. Bottom row: Predicted vs exact Diffusion $D_3(z)$.*

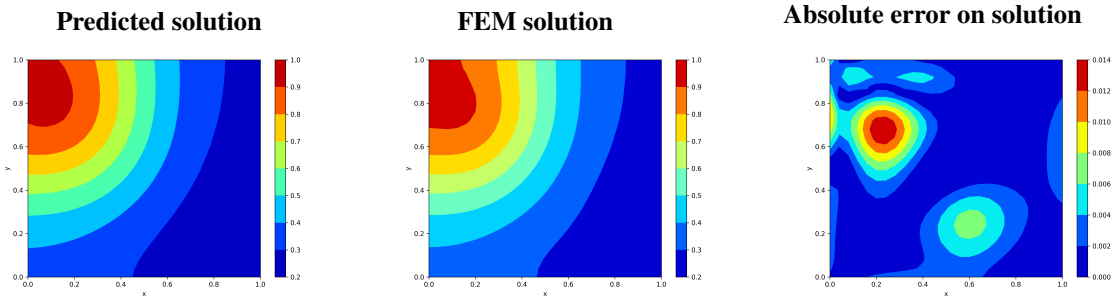


Figure 13: *Contour Plots of the Predicted (left) vs FEM Solution(middle) and the absolute error(right) of u at $t = 1$.*

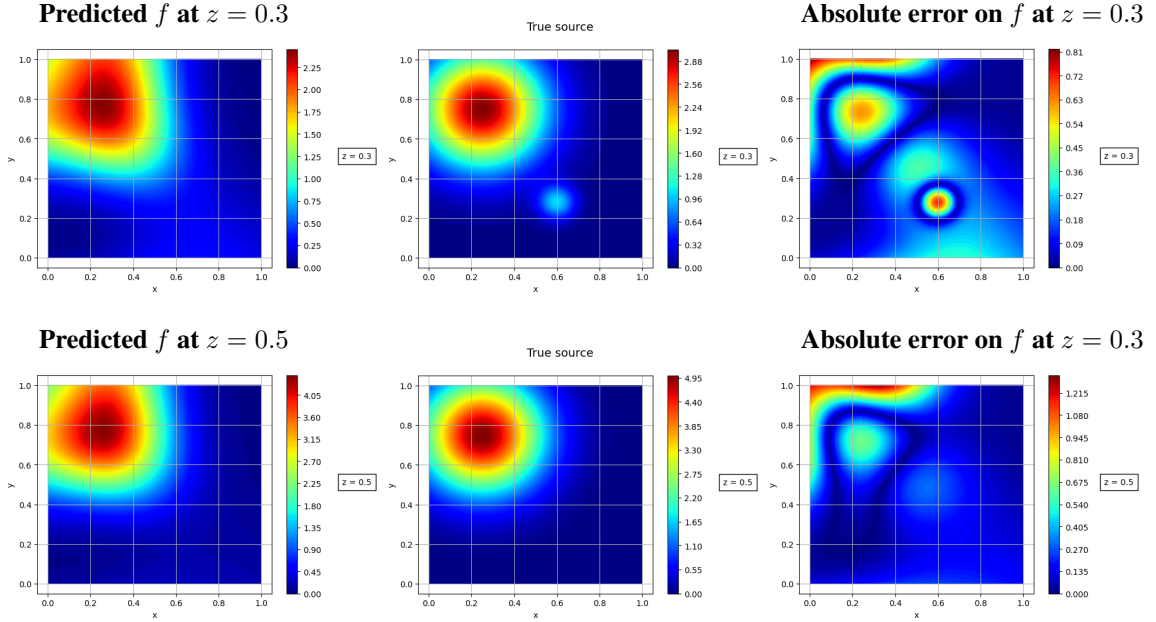


Figure 14: **Top row:** Contour plots of predicted (left), exact (middle) and absolute error (right) of the solution. **Middle row:** Contour plots of predicted (left), exact (middle) and absolute error (right) source function (bottom) at the altitude $z = 0.3$. **Bottom row:** Contour plots of predicted (left), exact (middle) and absolute error (right) source function (bottom) at the altitude $z = 0.5$.

6 Conclusion

This weighted adaptive method based on the neural tangent kernel of PINNs is presented in this paper as a promising approach to solve source inversion problems with parameters estimation from scarce data. This method has shown to be a robust method, achieving good performances in 2D and 3D advection diffusion equation with constants and non constants coefficients, despite the high ill-posedness of the problem. In our numerical results, we noticed that the approximation of the diffusion coefficient is the most challenging component compared to the velocity parameter, and this observation is addressed in [46] as a common observation in atmospheric dispersion. Consequently, there is a need of prior information on the diffusion parameter or increasing the number of measurements data for a better spatial coverage in order to expect an improvement in the approximation of the diffusion coefficients. We have also trained the same problem in a forward context with measurements data on the solution given to the model in addition to collocation points, and we observed a very slow convergence in the approximations as compared to its implementation in an inverse case, therefore illustrating how PINNs is best suited for inverse than forward problems. The reliability of our method was not considered in this work, and therefore in the future, we could incorporate uncertainty quantification to this approach in order to study the influence of the each parameters on the PINN model approximations.

Funding

This work was made possible by a grant from DeepMind Technologies Limited (provided through the African Institute for Mathematical Sciences). The statements made and views expressed are solely the responsibility of the authors. The authors sincerely thank the African Institute for Mathematical Sciences Research and Innovation for their support and resources provided during this research. BH was supported by the National Science Foundation grants DMS DMS-2337678, "CAREER: Gaussian Processes for Scientific Machine Learning: Theoretical Analysis and Computational Algorithms" and DMS-2208535 "Machine Learning for Bayesian Inverse Problems".

References

- [1] M Raissi, P Perdikaris, and GE Karniadakis. A deep learning framework for solving forward and inverse problems involving nonlinear partial differential equations. *J. Comput. Phys.*, 378:686–707, 2019.
- [2] George Em Karniadakis, Ioannis G Kevrekidis, Lu Lu, Paris Perdikaris, Sifan Wang, and Liu Yang. Physics-informed machine learning. *Nature Reviews Physics*, 3(6):422–440, 2021.

- [3] Jeremy Yu, Lu Lu, Xuhui Meng, and George Em Karniadakis. Gradient-enhanced physics-informed neural networks for forward and inverse pde problems. *Computer Methods in Applied Mechanics and Engineering*, 393:114823, 2022.
- [4] Zhengqi Zhang, Jing Li, and Bin Liu. Annealed adaptive importance sampling method in pinns for solving high dimensional partial differential equations. *Journal of Computational Physics*, 521:113561, 2025.
- [5] Zheyuan Hu, Khemraj Shukla, George Em Karniadakis, and Kenji Kawaguchi. Tackling the curse of dimensionality with physics-informed neural networks. *Neural Networks*, 176:106369, August 2024.
- [6] Geoffrey Ingram Taylor. I. eddy motion in the atmosphere. *Philosophical Transactions of the Royal Society of London. Series A, Containing Papers of a Mathematical or Physical Character*, 215(523-537):1–26, 1915.
- [7] John H Seinfeld and Spyros N Pandis. *Atmospheric chemistry and physics: from air pollution to climate change*. John Wiley & Sons, 2016.
- [8] B Addepalli, K Sikorski, ER Pardyjak, and MS Zhdanov. Source characterization of atmospheric releases using stochastic search and regularized gradient optimization. *Inverse Problems in Science and Engineering*, 19(8):1097–1124, 2011.
- [9] Juarez Azevedo, Gildeberto S Cardoso, and Leizer Schnitman. An adaptive monte carlo markov chain method applied to the flow involving self-similar processes in porous media. *Journal of Porous Media*, 17(3), 2014.
- [10] Juan G García, Bamdad Hosseini, and John M Stockie. Simultaneous model calibration and source inversion in atmospheric dispersion models. *Pure and Applied Geophysics*, 178:757–776, 2021.
- [11] Bamdad Hosseini and John M Stockie. Bayesian estimation of airborne fugitive emissions using a gaussian plume model. *Atmospheric Environment*, 141:122–138, 2016.
- [12] Bamdad Hosseini and John M Stockie. Estimating airborne particulate emissions using a finite-volume forward solver coupled with a bayesian inversion approach. *Computers & Fluids*, 154:27–43, 2017.
- [13] Youngdeok Hwang, Hang J Kim, Won Chang, Kyongmin Yeo, and Yongku Kim. Bayesian pollution source identification via an inverse physics model. *Computational Statistics & Data Analysis*, 134:76–92, 2019.
- [14] K. Shankar Rao. Source estimation methods for atmospheric dispersion. *Atmospheric Environment*, 41(33):6964–6973, October 2007.
- [15] Ian G Enting. *Inverse problems in atmospheric constituent transport*. Cambridge University Press, 2002.
- [16] Inanc Senocak, Nicolas W. Hengartner, Margaret B. Short, and W. Brent Daniel. Stochastic event reconstruction of atmospheric contaminant dispersion using bayesian inference. *Atmospheric Environment*, 42(33):7718–7727, October 2008.
- [17] Derek Wade and Inanc Senocak. Stochastic reconstruction of multiple source atmospheric contaminant dispersion events. *Atmospheric Environment*, 74:45–51, August 2013.
- [18] Roseane AS Albani and Vinicius VL Albani. Tikhonov-type regularization and the finite element method applied to point source estimation in the atmosphere. *Atmospheric Environment*, 211:69–78, 2019.
- [19] Roseane AS Albani and Vinicius VL Albani. An accurate strategy to retrieve multiple source emissions in the atmosphere. *Atmospheric Environment*, 233:117579, 2020.
- [20] Roseane AS Albani, Vinicius VL Albani, Hélio S Migon, and Antônio J Silva Neto. Uncertainty quantification and atmospheric source estimation with a discrepancy-based and a state-dependent adaptative mcmc. *Environmental Pollution*, 290:118039, 2021.
- [21] Zihan Huang, Yuan Wang, Qi Yu, Weichun Ma, Yan Zhang, and Limin Chen. Source area identification with observation from limited monitor sites for air pollution episodes in industrial parks. *Atmospheric Environment*, 122:1–9, 2015.
- [22] Gerard T Schuster, Yuqing Chen, and Shihang Feng. Review of physics-informed machine-learning inversion of geophysical data. *Geophysics*, 89(6):T337–T356, 2024.
- [23] Majid Rasht-Behesht, Christian Huber, Khemraj Shukla, and George Em Karniadakis. Physics-informed neural networks (pinns) for wave propagation and full waveform inversions. *Journal of Geophysical Research: Solid Earth*, 127(5):e2021JB023120, 2022.
- [24] Ivan Depina, Saket Jain, Sigurdur Mar Valsson, and Hrvoje Gotovac. Application of physics-informed neural networks to inverse problems in unsaturated groundwater flow. *Georisk: Assessment and Management of Risk for Engineered Systems and Geohazards*, 16(1):21–36, 2022.
- [25] Chao Song and Tariq A Alkhalifah. Wavefield reconstruction inversion via physics-informed neural networks. *IEEE Transactions on Geoscience and Remote Sensing*, 60:1–12, 2021.

- [26] Xinquan Huang and Tariq A Alkhalifah. Microseismic source imaging using physics-informed neural networks with hard constraints. *IEEE Transactions on Geoscience and Remote Sensing*, 62:1–11, 2024.
- [27] Dongjin Kim and Jaewook Lee. A review of physics informed neural networks for multiscale analysis and inverse problems. *Multiscale Science and Engineering*, 6(1):1–11, 2024.
- [28] Ameya D Jagtap, Zhiping Mao, Nikolaus Adams, and George Em Karniadakis. Physics-informed neural networks for inverse problems in supersonic flows. *Journal of Computational Physics*, 466:111402, 2022.
- [29] Tarik Sahin, Max von Danwitz, and Alexander Popp. Solving forward and inverse problems of contact mechanics using physics-informed neural networks. *Advanced Modeling and Simulation in Engineering Sciences*, 11(1):11, 2024.
- [30] Zhao Chen, Yang Liu, and Hao Sun. Physics-informed learning of governing equations from scarce data. *Nature communications*, 12(1):6136, 2021.
- [31] Yasamin Jalalian, Juan Felipe Osorio Ramirez, Alexander Hsu, Bamdad Hosseini, and Houman Owhadi. Data-efficient kernel methods for learning differential equations and their solution operators: Algorithms and error analysis. *arXiv preprint arXiv:2503.01036*, 2025.
- [32] Yasamin Jalalian, Mostafa Samir, Boumediene Hamzi, Peyman Tavallali, and Houman Owhadi. Data-efficient kernel methods for learning hamiltonian systems. *arXiv preprint arXiv:2509.17154*, 2025.
- [33] Samuel H Rudy, Steven L Brunton, Joshua L Proctor, and J Nathan Kutz. Data-driven discovery of partial differential equations. *Science advances*, 3(4):e1602614, 2017.
- [34] Sifan Wang, Yujun Teng, and Paris Perdikaris. Understanding and mitigating gradient flow pathologies in physics-informed neural networks. *SIAM Journal on Scientific Computing*, 43(5):A3055–A3081, 2021.
- [35] Dehao Liu and Yan Wang. A dual-dimer method for training physics-constrained neural networks with minimax architecture. *Neural Networks*, 136:112–125, 2021.
- [36] Colby L Wight and Jia Zhao. Solving allen-cahn and cahn-hilliard equations using the adaptive physics informed neural networks. *arXiv preprint arXiv:2007.04542*, 2020.
- [37] Levi McClenny Ulisses Braga-Neto. Self-adaptive physics-informed neural networks using a soft attention mechanism. 2021.
- [38] Sifan Wang, Xinling Yu, and Paris Perdikaris. When and why pinns fail to train: A neural tangent kernel perspective. *Journal of Computational Physics*, 449:110768, 2022.
- [39] Arthur Jacot, Franck Gabriel, and Clément Hongler. Neural tangent kernel: Convergence and generalization in neural networks. *Advances in neural information processing systems*, 31, 2018.
- [40] Sifan Wang, Hanwen Wang, and Paris Perdikaris. On the eigenvector bias of fourier feature networks: From regression to solving multi-scale pdes with physics-informed neural networks. *Computer Methods in Applied Mechanics and Engineering*, 384:113938, 2021.
- [41] Salah A Faroughi and Farinaz Mostajeran. Neural tangent kernel analysis to probe convergence in physics-informed neural solvers: Pikans vs. pinns. *arXiv preprint arXiv:2506.07958*, 2025.
- [42] Dietrich Braess. *Finite elements: Theory, fast solvers, and applications in solid mechanics*. Cambridge University Press, 2001.
- [43] John C Strikwerda. *Finite difference schemes and partial differential equations*. SIAM, 2004.
- [44] Maziar Raissi, Paris Perdikaris, and George Em Karniadakis. Physics informed deep learning (part i): Data-driven solutions of nonlinear partial differential equations. *arXiv preprint arXiv:1711.10561*, 2017.
- [45] Lu Lu, Xuhui Meng, Zhiping Mao, and George Em Karniadakis. Deepxde: A deep learning library for solving differential equations. *SIAM review*, 63(1):208–228, 2021.
- [46] John M Stockie. The mathematics of atmospheric dispersion modeling. *Siam Review*, 53(2):349–372, 2011.
- [47] Jin-Sheng Lin and Lynn M Hildemann. Analytical solutions of the atmospheric diffusion equation with multiple sources and height-dependent wind speed and eddy diffusivities. *Atmospheric Environment*, 30(2):239–254, 1996.
- [48] Bamdad Hosseini and John M Stockie. Airborne contaminant source estimation using a finite-volume forward solver coupled with a bayesian inversion approach. *arXiv preprint arXiv:1607.03518*, 2016.
- [49] S Pal Arya et al. *Air pollution meteorology and dispersion*, volume 310. Oxford University Press New York, 1999.

A Proof of lemma1

Proof 1 We recall the loss function to minimize:

$$\mathcal{L}(\Theta) = \lambda_r \mathcal{L}_r(\Theta) + \lambda_b \mathcal{L}_b(\theta_u) + \lambda_z \mathcal{L}_z(\theta_u), \quad \Theta = \{\theta_u, \theta_f, \gamma\} \quad (12)$$

and the gradient flow system $\frac{d\Theta(s)}{ds} = -\nabla_{\Theta} \mathcal{L}(\Theta(s))$, with $\Theta(s) = \{\theta_u(s), \theta_f(s), \gamma(s)\}$ which is explicitly written as

$$\begin{bmatrix} \frac{d\theta_u(s)}{ds} \\ \frac{d\theta_f(s)}{ds} \\ \frac{d\gamma(s)}{ds} \end{bmatrix} = - \begin{bmatrix} \nabla_{\theta_u} \mathcal{L}(\Theta(s)) \\ \nabla_{\theta_f} \mathcal{L}(\Theta(s)) \\ \nabla_{\gamma} \mathcal{L}(\Theta(s)) \end{bmatrix} \quad (13)$$

By replacing (12) in (13), we have

$$\begin{aligned} \frac{d\theta_u(s)}{ds} &= -\nabla_{\theta_u} \mathcal{L}(\Theta(s)) \\ &= -\frac{2\lambda_r}{N_r} \sum_{i=1}^{N_r} \left(\mathcal{F}[u(\mathbf{x}_r^i, t_r^i; \theta_u(s)); \gamma(s)] - f(\mathbf{x}_r^i, t_r^i, \theta_f(s)) \right) \frac{\partial \mathcal{F}[u(\mathbf{x}_r^i, t_r^i; \theta_u(s)); \gamma(s)]}{\partial \theta_u} \\ &\quad - \frac{2\lambda_b}{N_b} \sum_{i=1}^{N_b} \left(\mathcal{B}[u(\mathbf{x}_b^i, t_b^i; \theta_u(s)) - h(\mathbf{x}_b^i, t_b^i)] \right) \frac{\partial \mathcal{B}[u(\mathbf{x}_b^i, t_b^i; \theta_u(s))]}{\partial \theta_u} \\ &\quad - \frac{2\lambda_z}{N_z} \sum_{i=1}^{N_z} \left(\tau_i[u(\mathbf{x}_z^i, t_z^i; \theta_u(s)) - \mathbf{z}_i^*] \right) \frac{\partial \tau_i[u(\mathbf{x}_z^i, t_z^i; \theta_u(s))]}{\partial \theta_u} \end{aligned}$$

Similarly, we have

$$\begin{aligned} \frac{d\theta_f(s)}{ds} &= \frac{2\lambda_r}{N_r} \sum_{i=1}^{N_r} \left(\mathcal{F}[u(\mathbf{x}_r^i, t_r^i; \theta_u(s)); \gamma(s)] - f(\mathbf{x}_r^i, t_r^i, \theta_f(s)) \right) \frac{\partial f(\mathbf{x}_r^i, t_r^i, \theta_f(s))}{\partial \theta_f} \\ \frac{d\gamma(s)}{ds} &= -\frac{2\lambda_r}{N_r} \sum_{i=1}^{N_r} \left(\mathcal{F}[u(\mathbf{x}_r^i, t_r^i; \theta_u(s)); \gamma(s)] - f(\mathbf{x}_r^i, t_r^i, \theta_f(s)) \right) \frac{\partial \mathcal{F}[u(\mathbf{x}_r^i, t_r^i; \theta_u(s)); \gamma(s)]}{\partial \theta_f} \end{aligned}$$

For $0 \leq j \leq N_r$, we have

$$\begin{aligned} &\frac{d(\mathcal{F}[u(\mathbf{x}_r^j, t_r^j; \theta_u(s)); \gamma(s)] - f(\mathbf{x}_r^j, t_r^j, \theta_f(s)))}{ds} \\ &= \frac{d(\mathcal{F}[u(\mathbf{x}_r^j, t_r^j; \theta_u(s)); \gamma(s)] - f(\mathbf{x}_r^j, t_r^j, \theta_f(s)))}{d\Theta} \cdot \frac{d\Theta(s)}{ds} \\ &= \begin{bmatrix} \frac{d(\mathcal{F}[u(\mathbf{x}_r^j, t_r^j; \theta_u(s)); \gamma(s)] - f(\mathbf{x}_r^j, t_r^j, \theta_f(s)))}{d\theta_u} \\ \frac{d(\mathcal{F}[u(\mathbf{x}_r^j, t_r^j; \theta_u(s)); \gamma(s)] - f(\mathbf{x}_r^j, t_r^j, \theta_f(s)))}{d\theta_f} \\ \frac{d(\mathcal{F}[u(\mathbf{x}_r^j, t_r^j; \theta_u(s)); \gamma(s)] - f(\mathbf{x}_r^j, t_r^j, \theta_f(s)))}{d\gamma} \end{bmatrix} \cdot \begin{bmatrix} \frac{d\theta_u(s)}{ds} \\ \frac{d\theta_f(s)}{ds} \\ \frac{d\gamma(s)}{ds} \end{bmatrix} \\ &= \underbrace{\frac{d(\mathcal{F}[u(\mathbf{x}_r^j, t_r^j; \theta_u(s)); \gamma(s)])}{d\theta_u}}_A \times \frac{d\theta_u(s)}{ds} - \underbrace{\frac{d(f(\mathbf{x}_r^j, t_r^j, \theta_f(s)))}{d\theta_f}}_B \times \frac{d\theta_f(s)}{ds} \\ &\quad + \underbrace{\frac{d(\mathcal{F}[u(\mathbf{x}_r^j, t_r^j; \theta_u(s)); \gamma(s)])}{d\gamma}}_C \times \frac{d\gamma(s)}{ds} \\ &= A - B + C \end{aligned}$$

$$\begin{aligned}
A &= \frac{d(\mathcal{F}[u(\mathbf{x}_r^i, t_r^i; \boldsymbol{\theta}_u(s)); \gamma(s)]}{d\boldsymbol{\theta}_u} \left[-\frac{2\lambda_r}{N_r} \sum_{i=1}^{N_r} \left(\mathcal{F}[u(\mathbf{x}_r^i, t_r^i; \boldsymbol{\theta}_u(s)); \gamma(s)] - f(\mathbf{x}_r^i, t_r^i, \boldsymbol{\theta}_f(s)) \right) \right. \\
&\times \frac{\partial \mathcal{F}[u(\mathbf{x}_r^i, t_r^i; \boldsymbol{\theta}_u(s)); \gamma(s)]}{\partial \boldsymbol{\theta}_u} - \frac{2\lambda_b}{N_b} \sum_{i=1}^{N_b} \left(\mathcal{B}[u(\mathbf{x}_b^i, t_b^i; \boldsymbol{\theta}_u(s)) - h(\mathbf{x}_b^i, t_b^i)] \right) \frac{\partial \mathcal{B}[u(\mathbf{x}_b^i, t_b^i; \boldsymbol{\theta}_u(s))]}{\partial \boldsymbol{\theta}_u} \\
&- \left. \frac{2\lambda_z}{N_z} \sum_{i=1}^{N_z} \left(\tau_i[u(\mathbf{x}_z^i, t_z^i; \boldsymbol{\theta}_u(s)) - \mathbf{z}_i^*] \right) \frac{\partial \tau_i[u(\mathbf{x}_z^i, t_z^i; \boldsymbol{\theta}_u(s))]}{\partial \boldsymbol{\theta}_u} \right] \\
&= -\frac{2\lambda_r}{N_r} \sum_{i=1}^{N_r} \left(\mathcal{F}[u(\mathbf{x}_r^i, t_r^i; \boldsymbol{\theta}_u(s)); \gamma(s)] - f(\mathbf{x}_r^i, t_r^i, \boldsymbol{\theta}_f(s)) \right) \\
&\times \left\langle \frac{\partial(\mathcal{F}[u(\mathbf{x}_r^i, t_r^i; \boldsymbol{\theta}_u(s)); \gamma(s)]}{\partial \boldsymbol{\theta}_u}, \frac{\partial(\mathcal{F}[u(\mathbf{x}_r^j, t_r^j; \boldsymbol{\theta}_u(s)); \gamma(s)]}{\partial \boldsymbol{\theta}_u} \right\rangle \\
&- \frac{2\lambda_b}{N_b} \sum_{i=1}^{N_b} (\mathcal{B}[u(\mathbf{x}_b^i, t_b^i; \boldsymbol{\theta}_u(s)) - h(\mathbf{x}_b^i, t_b^i)]) \left\langle \frac{\partial \mathcal{B}[u(\mathbf{x}_b^i, t_b^i; \boldsymbol{\theta}_u(s))]}{\partial \boldsymbol{\theta}_u}, \frac{\partial(\mathcal{F}[u(\mathbf{x}_r^j, t_r^j; \boldsymbol{\theta}_u(s)); \gamma(s)]}{\partial \boldsymbol{\theta}_u} \right\rangle \\
&- \frac{2\lambda_z}{N_z} \sum_{i=1}^{N_z} (\tau_i[u(\mathbf{x}_z^i, t_z^i; \boldsymbol{\theta}_u(s)) - \mathbf{z}_i^*]) \left\langle \frac{\partial \tau_i[u(\mathbf{x}_z^i, t_z^i; \boldsymbol{\theta}_u(s))]}{\partial \boldsymbol{\theta}_u}, \frac{\partial(\mathcal{F}[u(\mathbf{x}_r^j, t_r^j; \boldsymbol{\theta}_u(s)); \gamma(s)]}{\partial \boldsymbol{\theta}_u} \right\rangle \\
&= -\frac{2\lambda_r}{N_r} \sum_{i=1}^{N_r} \left(\mathcal{F}[u(\mathbf{x}_r^i, t_r^i; \boldsymbol{\theta}_u(s)); \gamma(s)] - f(\mathbf{x}_r^i, t_r^i, \boldsymbol{\theta}_f(s)) \right) (J_{rr}^{\boldsymbol{\theta}_u})_{ij} \\
&- \frac{2\lambda_b}{N_b} \sum_{i=1}^{N_b} (\mathcal{B}[u(\mathbf{x}_b^i, t_b^i; \boldsymbol{\theta}_u(s)) - h(\mathbf{x}_b^i, t_b^i)]) (\mathbf{K}_{br}^{\boldsymbol{\theta}_u})_{ij} - \frac{2\lambda_z}{N_z} \sum_{i=1}^{N_z} (\tau_i[u(\mathbf{x}_z^i, t_z^i; \boldsymbol{\theta}_u(s)) - \mathbf{z}_i^*]) (\mathbf{K}_{zr}^{\boldsymbol{\theta}_u})_{ij} \\
B &= \frac{d(f(\mathbf{x}_r^j, t_r^j), \boldsymbol{\theta}_f(s))}{d\boldsymbol{\theta}_f} \left[\frac{2\lambda_r}{N_r} \sum_{i=1}^{N_r} \left(\mathcal{F}[u(\mathbf{x}_r^i, t_r^i; \boldsymbol{\theta}_u(s)); \gamma(s)] - f(\mathbf{x}_r^i, t_r^i, \boldsymbol{\theta}_f(s)) \right) \frac{\partial f(\mathbf{x}_r^j, t_r^j, \boldsymbol{\theta}_f(s))}{\partial \boldsymbol{\theta}_f} \right] \\
&= \frac{2\lambda_r}{N_r} \sum_{i=1}^{N_r} \left(\mathcal{F}[u(\mathbf{x}_r^i, t_r^i; \boldsymbol{\theta}_u(s)); \gamma(s)] - f(\mathbf{x}_r^i, t_r^i, \boldsymbol{\theta}_f(s)) \right) \left\langle \frac{\partial f(\mathbf{x}_r^i, t_r^i, \boldsymbol{\theta}_f(s))}{\partial \boldsymbol{\theta}_f}, \frac{\partial f(\mathbf{x}_r^j, t_r^j, \boldsymbol{\theta}_f(s))}{\partial \boldsymbol{\theta}_f} \right\rangle \\
&= \frac{2\lambda_r}{N_r} \sum_{i=1}^{N_r} \left(\mathcal{F}[u(\mathbf{x}_r^i, t_r^i; \boldsymbol{\theta}_u(s)); \gamma(s)] - f(\mathbf{x}_r^i, t_r^i, \boldsymbol{\theta}_f(s)) \right) (J_{rr}^{\boldsymbol{\theta}_f})_{ji} \\
C &= -\frac{2\lambda_r}{N_r} \sum_{i=1}^{N_r} \left(\mathcal{F}[u(\mathbf{x}_r^i, t_r^i; \boldsymbol{\theta}_u(s)); \gamma(s)] - f(\mathbf{x}_r^i, t_r^i, \boldsymbol{\theta}_f(s)) \right) \\
&\times \left\langle \frac{\partial(\mathcal{F}[u(\mathbf{x}_r^i, t_r^i; \boldsymbol{\theta}_u(s)); \gamma(s)]}{\partial \gamma}, \frac{\partial(\mathcal{F}[u(\mathbf{x}_r^j, t_r^j; \boldsymbol{\theta}_u(s)); \gamma(s)]}{\partial \gamma} \right\rangle
\end{aligned}$$

Therefore we have

$$\begin{aligned}
& \frac{d(\mathcal{F}[u(\mathbf{x}_r^j, t_r^j; \boldsymbol{\theta}_u(s)); \gamma(s)] - f(\mathbf{x}_r^j, t_r^j, \boldsymbol{\theta}_f(s)))}{ds} \\
&= -\frac{2\lambda_r}{N_r} \sum_{i=1}^{N_r} (\mathcal{F}[u(\mathbf{x}_r^i, t_r^i; \boldsymbol{\theta}_u(s)); \gamma(s)] - f(\mathbf{x}_r^i, t_r^i, \boldsymbol{\theta}_f(s))) \left((J_{rr}^{\boldsymbol{\theta}_u}(s))_{ij} + (J_{rr}^{\boldsymbol{\theta}_f}(s))_{ij} + (J_{rr}^\gamma(s))_{ij} \right) \\
&\quad - \frac{2\lambda_b}{N_b} \sum_{i=1}^{N_b} (\mathcal{B}[u(\mathbf{x}_b^i, t_b^i; \boldsymbol{\theta}_u(s)) - h(\mathbf{x}_b^i, t_b^i)])(\mathbf{K}_{rb}^{\boldsymbol{\theta}_u})_{ij} - \frac{2\lambda_z}{N_z} \sum_{i=1}^{N_z} (\tau_i[u(\mathbf{x}_z^i, t_z^i; \boldsymbol{\theta}_u(s)) - \mathbf{z}_i^*])(\mathbf{K}_{rz}^{\boldsymbol{\theta}_u})_{ij} \\
&= -\frac{2\lambda_r}{N_r} \sum_{i=1}^{N_r} (\mathcal{F}[u(\mathbf{x}_r^i, t_r^i; \boldsymbol{\theta}_u(s)); \gamma(s)] - f(\mathbf{x}_r^i, t_r^i, \boldsymbol{\theta}_f(s))) \\
&\quad \times \left\langle \left(\frac{\partial(\mathcal{F}[u(\mathbf{x}_r^i, t_r^i; \boldsymbol{\theta}_u(s)); \gamma(s)])}{\partial \boldsymbol{\theta}_u} \right), \left(\frac{\partial(\mathcal{F}[u(\mathbf{x}_r^i, t_r^i; \boldsymbol{\theta}_u(s)); \gamma(s)])}{\partial \boldsymbol{\theta}_f} \right) \right\rangle \\
&\quad - \frac{2\lambda_b}{N_b} \sum_{i=1}^{N_b} (\mathcal{B}[u(\mathbf{x}_b^i, t_b^i; \boldsymbol{\theta}_u(s)) - h(\mathbf{x}_b^i, t_b^i)])(\mathbf{K}_{br}^{\boldsymbol{\theta}_u})_{ij} - \frac{2\lambda_z}{N_z} \sum_{i=1}^{N_z} (\tau_i[u(\mathbf{x}_z^i, t_z^i; \boldsymbol{\theta}_u(s)) - \mathbf{z}_i^*])(\mathbf{K}_{zr}^{\boldsymbol{\theta}_u})_{ij} \\
&= \frac{d\mathcal{L}_r(\boldsymbol{\Theta}(s))}{dt}
\end{aligned}$$

and we denote $(\mathbf{K}_{rr}(s))_{ij} = \left\langle \left(\frac{\partial(\mathcal{F}[u(\mathbf{x}_r^i, t_r^i; \boldsymbol{\theta}_u(s)); \gamma(s)])}{\partial \boldsymbol{\theta}_u} \right), \left(\frac{\partial(\mathcal{F}[u(\mathbf{x}_r^j, t_r^j; \boldsymbol{\theta}_u(s)); \gamma(s)])}{\partial \boldsymbol{\theta}_f} \right) \right\rangle$ For $0 \leq j \leq N_b$, we have

$$\frac{d\mathcal{B}[u(\mathbf{x}_b^j, t_b^j; \boldsymbol{\theta}_u(s))]}{ds} = \frac{d\mathcal{B}[u(\mathbf{x}_b^j, t_b^j; \boldsymbol{\theta}_u(s))]}{d\boldsymbol{\theta}} \times \frac{d\boldsymbol{\theta}(s)}{ds} = \frac{d\mathcal{B}[u(\mathbf{x}_b^j, t_b^j; \boldsymbol{\theta}_u(s))]}{d\boldsymbol{\theta}_u} \times \frac{d\boldsymbol{\theta}_u(s)}{ds}$$

$$\begin{aligned}
&= \frac{d\mathcal{B}[u(\mathbf{x}_b^j, t_b^j; \boldsymbol{\theta}_u(s))]}{d\boldsymbol{\theta}_u} \left[-\frac{2\lambda_r}{N_r} \sum_{i=1}^{N_r} \left(\mathcal{F}[u(\mathbf{x}_r^i, t_r^i; \boldsymbol{\theta}_u(s)); \gamma(s)] - f(\mathbf{x}_r^i, t_r^i, \boldsymbol{\theta}_f(s)) \right) \right. \\
&\times \frac{\partial(\mathcal{F}[u(\mathbf{x}_r^i, t_r^i; \boldsymbol{\theta}_u(s)); \gamma(s)])}{\partial\boldsymbol{\theta}_u} \\
&- \frac{2\lambda_b}{N_b} \sum_{i=1}^{N_b} (\mathcal{B}[u(\mathbf{x}_b^i, t_b^i; \boldsymbol{\theta}_u(s)) - h(\mathbf{x}_b^i, t_b^i)]) \frac{\partial\mathcal{B}[u(\mathbf{x}_b^i, t_b^i; \boldsymbol{\theta}_u(s))]}{\partial\boldsymbol{\theta}_u} \\
&\left. - \frac{2\lambda_z}{N_z} \sum_{i=1}^{N_z} (\tau_i[u(\mathbf{x}_z^i, t_z^i; \boldsymbol{\theta}_u(s)) - \mathbf{z}_i^*]) \frac{\partial\tau_i[u(\mathbf{x}_z^i, t_z^i; \boldsymbol{\theta}_u(s))]}{\partial\boldsymbol{\theta}_u} \right] \\
&= -\frac{2\lambda_r}{N_r} \sum_{i=1}^{N_r} (\mathcal{F}[u(\mathbf{x}_r^i, t_r^i; \boldsymbol{\theta}_u(s)); \gamma(s)] - f(\mathbf{x}_r^i, t_r^i, \boldsymbol{\theta}_f(s))) \\
&\times \left\langle \frac{d(\mathcal{F}[u(\mathbf{x}_r^i, t_r^i; \boldsymbol{\theta}_u(s)); \gamma(s)])}{d\boldsymbol{\theta}_u}, \frac{d\mathcal{B}[u(\mathbf{x}_b^j, t_b^j; \boldsymbol{\theta}_u(s))]}{d\boldsymbol{\theta}_u} \right\rangle \\
&- \frac{2\lambda_b}{N_b} \sum_{i=1}^{N_b} (\mathcal{B}[u(\mathbf{x}_b^i, t_b^i; \boldsymbol{\theta}_u(s)) - h(\mathbf{x}_b^i, t_b^i)]) \left\langle \frac{d\mathcal{B}[u(\mathbf{x}_b^i, t_b^i; \boldsymbol{\theta}_u(s))]}{d\boldsymbol{\theta}_u}, \frac{d\mathcal{B}[u(\mathbf{x}_b^j, t_b^j; \boldsymbol{\theta}_u(s))]}{d\boldsymbol{\theta}_u} \right\rangle \\
&- \frac{2\lambda_z}{N_z} \sum_{i=1}^{N_z} (\tau_i[u(\mathbf{x}_z^i, t_z^i; \boldsymbol{\theta}_u(s)) - \mathbf{z}_i^*]) \left\langle \frac{d\tau_i[u(\mathbf{x}_z^i, t_z^i; \boldsymbol{\theta}_u(s))]}{d\boldsymbol{\theta}_u}, \frac{d\mathcal{B}[u(\mathbf{x}_b^j, t_b^j; \boldsymbol{\theta}_u(s))]}{d\boldsymbol{\theta}_u} \right\rangle \\
&= -\frac{2\lambda_r}{N_r} \sum_{i=1}^{N_r} (\mathcal{F}[u(\mathbf{x}_r^i, t_r^i; \boldsymbol{\theta}_u(s)); \gamma(s)] - f(\mathbf{x}_r^i, t_r^i, \boldsymbol{\theta}_f(s))) (\mathbf{K}_{rb}(s))_{ij} \\
&- \frac{2\lambda_b}{N_b} \sum_{i=1}^{N_b} (\mathcal{B}[u(\mathbf{x}_b^i, t_b^i; \boldsymbol{\theta}_u(s)) - h(\mathbf{x}_b^i, t_b^i)]) (\mathbf{K}_{bb}^{\boldsymbol{\theta}_u}(s))_{ij} \\
&- \frac{2\lambda_z}{N_z} \sum_{i=1}^{N_z} (\tau_i[u(\mathbf{x}_z^i, t_z^i; \boldsymbol{\theta}_u(s)) - \mathbf{z}_i^*]) (\mathbf{K}_{zb}^{\boldsymbol{\theta}_u}(s))_{ij} \\
&= \frac{d\mathcal{L}_b(\boldsymbol{\theta}_u)}{ds}
\end{aligned}$$

For $0 \leq j \leq N_z$, we have

$$\begin{aligned}
& \frac{d\tau_j[u(\mathbf{x}_b^j, t_b^j; \boldsymbol{\theta}_u(s))]}{ds} \\
&= \frac{d\tau_j[u(\mathbf{x}_b^j, t_b^j; \boldsymbol{\theta}_u(s))]}{d\boldsymbol{\theta}_u} \times \frac{d\boldsymbol{\theta}_u(s)}{ds} \\
&= \frac{d\tau_j[u(\mathbf{x}_b^j, t_b^j; \boldsymbol{\theta}_u(s))]}{d\boldsymbol{\theta}_u} \left[-\frac{2\lambda_r}{N_r} \sum_{i=1}^{N_r} \left(\mathcal{F}[u(\mathbf{x}_r^i, t_r^i; \boldsymbol{\theta}_u(s)); \gamma(s)] - f(\mathbf{x}_r^i, t_r^i; \boldsymbol{\theta}_f(s)) \right) \right. \\
&\quad \times \frac{\partial(\mathcal{F}[u(\mathbf{x}_r^i, t_r^i; \boldsymbol{\theta}_u(s)); \gamma(s)] - f(\mathbf{x}_r^i, t_r^i; \boldsymbol{\theta}_f(s)))}{\partial\boldsymbol{\theta}_u} \\
&\quad - \frac{2\lambda_b}{N_b} \sum_{i=1}^{N_b} (\mathcal{B}[u(\mathbf{x}_b^i, t_b^i; \boldsymbol{\theta}_u(s)) - h(\mathbf{x}_b^i, t_b^i)]) \frac{\partial\mathcal{B}[u(\mathbf{x}_b^i, t_b^i; \boldsymbol{\theta}_u(s))]}{\partial\boldsymbol{\theta}_u} \\
&\quad \left. - \frac{2\lambda_z}{N_z} \sum_{i=1}^{N_z} (\tau_i[u(\mathbf{x}_z^i, t_z^i; \boldsymbol{\theta}_u(s)) - \mathbf{z}_i^*]) \frac{\partial\tau_i[u(\mathbf{x}_z^i, t_z^i; \boldsymbol{\theta}_u(s))]}{\partial\boldsymbol{\theta}_u} \right] \\
&= -\frac{2\lambda_r}{N_r} \sum_{i=1}^{N_r} (\mathcal{F}[u(\mathbf{x}_r^i, t_r^i; \boldsymbol{\theta}_u(s)); \gamma(s)] - f(\mathbf{x}_r^i, t_r^i; \boldsymbol{\theta}_f(s))) \\
&\quad \times \left\langle \frac{d(\mathcal{F}[u(\mathbf{x}_r^j, t_r^j; \boldsymbol{\theta}_u(s)); \gamma(s)] - f(\mathbf{x}_r^i, t_r^i; \boldsymbol{\theta}_f(s)))}{d\boldsymbol{\theta}_u}, \frac{d\tau_j[u(\mathbf{x}_b^j, t_b^j; \boldsymbol{\theta}_u(s))]}{d\boldsymbol{\theta}_u} \right\rangle \\
&\quad - \frac{2\lambda_b}{N_b} \sum_{i=1}^{N_b} (\mathcal{B}[u(\mathbf{x}_b^i, t_b^i; \boldsymbol{\theta}_u(s)) - h(\mathbf{x}_b^i, t_b^i)]) \left\langle \frac{d\mathcal{B}[u(\mathbf{x}_b^i, t_b^i; \boldsymbol{\theta}_u(s))]}{d\boldsymbol{\theta}_u}, \frac{d\tau_j[u(\mathbf{x}_b^j, t_b^j; \boldsymbol{\theta}_u(s))]}{d\boldsymbol{\theta}_u} \right\rangle \\
&\quad - \frac{2\lambda_z}{N_z} \sum_{i=1}^{N_z} (\tau_i[u(\mathbf{x}_z^i, t_z^i; \boldsymbol{\theta}_u(s)) - \mathbf{z}_i^*]) \left\langle \frac{d\tau_i[u(\mathbf{x}_z^i, t_z^i; \boldsymbol{\theta}_u(s))]}{d\boldsymbol{\theta}_u}, \frac{d\tau_j[u(\mathbf{x}_b^j, t_b^j; \boldsymbol{\theta}_u(s))]}{d\boldsymbol{\theta}_u} \right\rangle \\
&= -\frac{2\lambda_r}{N_r} \sum_{i=1}^{N_r} (\mathcal{F}[u(\mathbf{x}_r^i, t_r^i; \boldsymbol{\theta}_u(s)); \gamma(s)] - f(\mathbf{x}_r^i, t_r^i; \boldsymbol{\theta}_f(s))) (\mathbf{K}_{rz}^{\boldsymbol{\theta}_u}(s))_{ij} \\
&\quad - \frac{2\lambda_b}{N_b} \sum_{i=1}^{N_b} (\mathcal{B}[u(\mathbf{x}_b^i, t_b^i; \boldsymbol{\theta}_u(s)) - h(\mathbf{x}_b^i, t_b^i)]) \mathbf{K}_{bz}^{\boldsymbol{\theta}_u}(s) - \frac{2\lambda_z}{N_z} \sum_{i=1}^{N_z} (\tau_i[u(\mathbf{x}_z^i, t_z^i; \boldsymbol{\theta}_u(s)) - \mathbf{z}_i^*]) \mathbf{K}_{zz}^{\boldsymbol{\theta}_u}(s) \\
&= \frac{d\mathcal{L}_z(\boldsymbol{\theta}_u(s))}{ds}.
\end{aligned}$$

B Numerical results on the variation of Noise for the 2D ADE with constant coefficients using pointwise and accumulative observations

We observe on the figure 1 the random chosen measurements locations are not too close to the regions with high emission rate, but despite that, the variation of noise and the high-ill-posedness of our problem, we can deduce from the results in the figures 16, 18, 17 that in such a scenario the proposed PINNs approach can still exhibit good performances in identifying the location of high emission rate and recovering the solution of the .

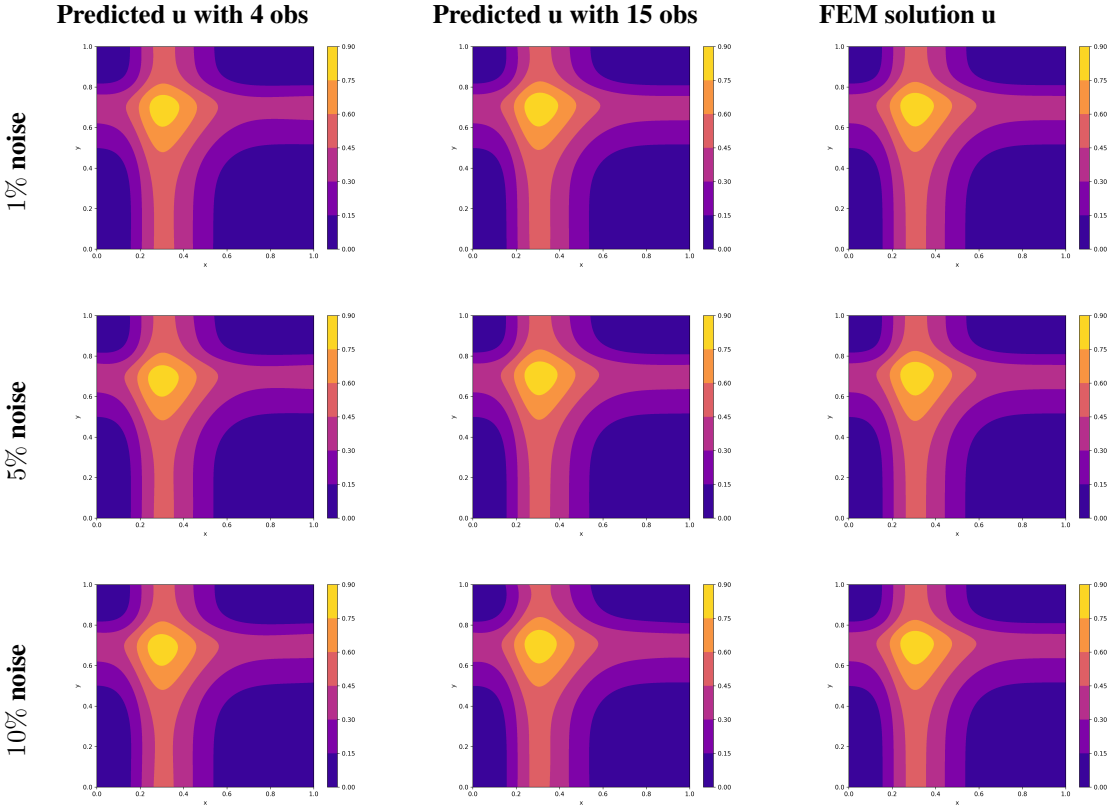


Figure 15: Predicted solution u at $t = 1$ vs FEM solution (Third column) using with 4 (First column) and 15 pointwise observations (Second column) with 1%, 5% and 10% of noise respectively.

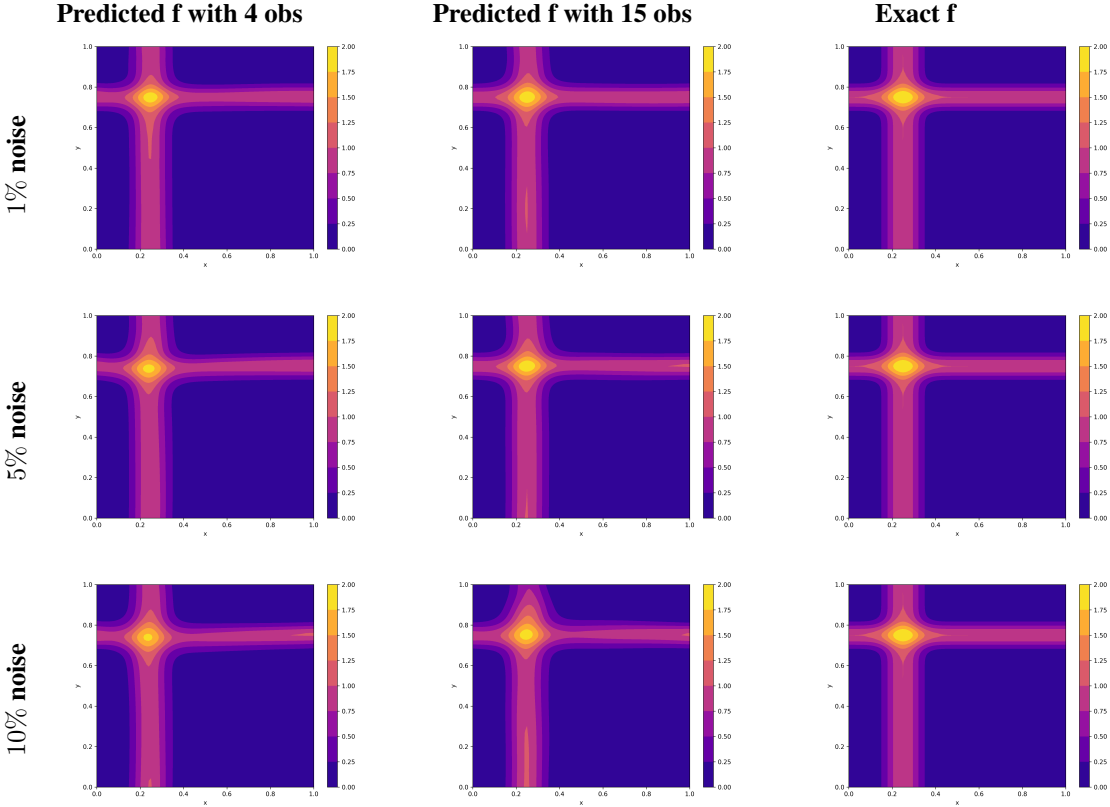


Figure 16: Predicted source function f vs exact f (Third column) using 4 (First column) and 15 pointwise observations (Second column) with 1%, 5% and 10% of noise respectively and the observation operator assumed to be an identity operator

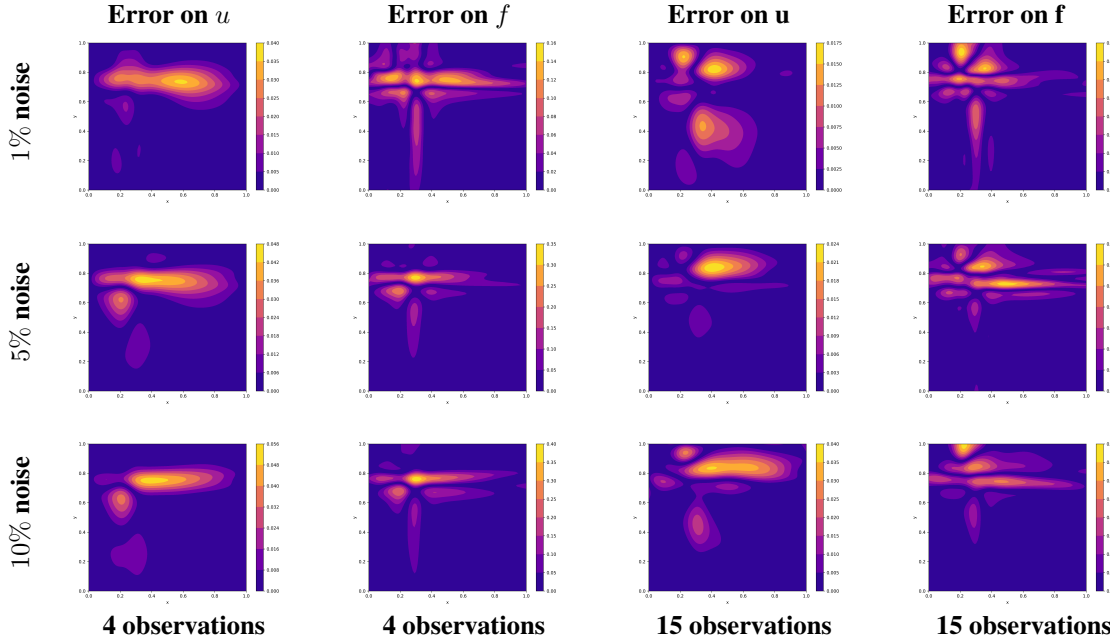


Figure 17: Contour plots of the absolute error on u at $t = 1$ and f with 1%, 5% and 10% of noise on pointwise observations.

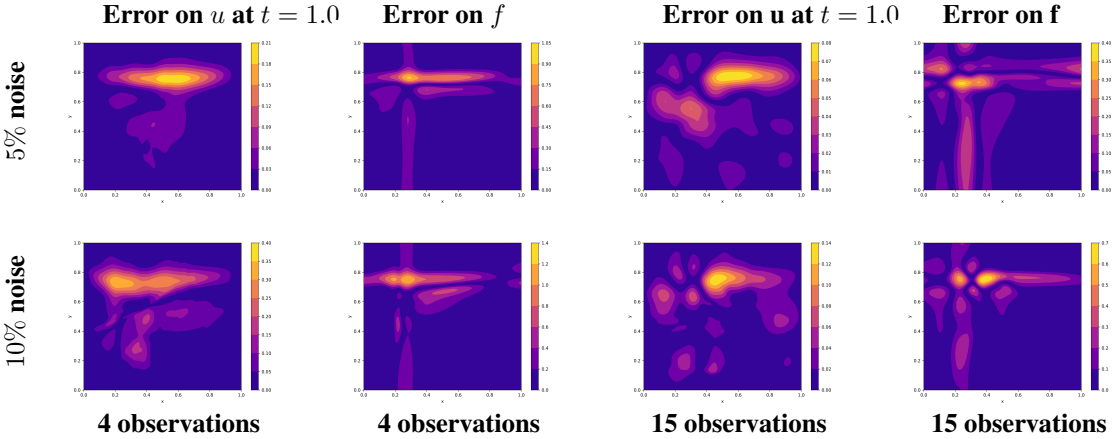


Figure 18: Contour plots of the absolute error on u at $t = 1$ and f with 5% and 10% of noise on 4 and 15 accumulative observations.